CHAPTER 2

INTRAMOLECULAR NUCLEAR FLUX DENSITIES

I. Barth[*,†,‡], C. Daniel[§], E. Gindensperger[§],
J. Manz[*,¶,‖], J. F. Pérez-Torres[¶], A. Schild[¶,‡],
C. Stemmle[¶], D. Sulzer[§] and Y. Yang[*]

The topic of this survey article has seen a renaissance during the past couple of years. Here we present and extend the results for various phenomena which we have published from 2012–2014, with gratitude to our coauthors. The new phenomena include (a) the first reduced nuclear flux densities in vibrating diatomic molecules or ions which have been deduced from experimental pump–probe spectra; these "experimental" nuclear flux densities reveal several quantum effects including (b) the "quantum accordion", i.e., during the turn from bond stretch to bond compression, the diatomic system never stands still — instead, various parts of it with different bond lengths flow into opposite directions. (c) Wavepacket interferometry has been extended from nuclear densities to flux densities, again revealing new phenomena: For example, (d) a vibrating nuclear wave function with compact initial shape may split into two partial waves which run into opposite directions, thus causing interfering flux densities. (e) Tunneling in symmetric 1-dimensional double-well systems yields maximum values of the associated nuclear flux density just below the potential barrier; this is in marked contrast with negligible values of the nuclear density just below the barrier. (f) Nuclear flux densities of pseudorotating nuclei may induce huge magnetic fields. A common methodologic theme of all topics is the continuity equation which connects the time derivative of the nuclear density to the divergence of the flux density, subject

[*]State Key Laboratory of Quantum Optics and Quantum Optics Devices, Institute of Laser Spectroscopy, Shanxi University, Taiyuan 030006, China
[†]Institut für Theoretische Physik, Leibniz Universität Hannover, 30167 Hannover, Germany
[‡]Max-Planck-Institut für Mikrostrukturphysik, 06120 Halle, Germany
[§]Laboratoire de Chimie Quantique, UMR 7177 CNRS/Université de Strasbourg, Institut de Chimie de Strasbourg, 67008 Strasbourg, France
[¶]Institut für Chemie und Biochemie, Freie Universität Berlin, 14195 Berlin, Germany
[‖]jmanz@chemie.fu-berlin.de

to the proper boundary conditions. (g) Nearly identical nuclear densities with different boundary conditions may be related to entirely different flux densities, e.g., during tunneling in cyclic versus non-cyclic systems. The original continuity equation, density and flux density of all nuclei, or of all nuclear degrees of freedom, may be reduced to the corresponding quantities for just a single nucleus, or just a single degree of freedom.

1. Introduction

When molecules vibrate or react, their nuclei and electrons flow. The corresponding observables are the intramolecular nuclear and electronic flux densities, respectively. The general quantum definition of flux densities was given already by Schrödinger, in the original paper which introduced the Schrödinger equation;[1] today it is in the textbooks and monographs.[2,3] Here we center attention on phenomena of nuclear flux densities within moving molecules which have been discovered during the years 2012–2014,[4–10] see also Refs. 11–19. These are complementary to intramolecular electronic flux densities,[13–16,18–36] and also to translational molecular flux densities in molecular beams.[37,38] More specifically, we shall focus on time-dependent intramolecular nuclear flux densities which accompany unimolecular processes such as isomerizations, or just vibrations. These may evolve in the femtosecond time domain. This could not be monitored by Schrödinger's contemporaries. The general topic of intramolecular flux densities thus became a sleeping beauty, for decades. The present specific topic of intramolecular nuclear flux densities was awakened indirectly by theoreticians who carried out quantum model simulations in neighboring fields, either for nuclear flux densities during bimolecular reactions,[39] inelastic collisions[40] or photodissociations,[41] or for intramolecular electronic flux densities induced by magnetic fields,[20–22] and finally for electronic flux densities of ring currents in highly symmetric molecules which are excited to degenerate electronic states by means of circularly polarized laser pulses,[23–27,42] or for bond currents induced by two coherent linearly polarized laser pulses.[36] The laser driven intramolecular electronic flux densities[23–27] turned out to be about two orders of magnitude stronger than those induced by traditional static magnetic fields.[20–22] These rather strong effects[23–27] stimulated searches for analogous phenomena in nuclear flux densities of pseudorotating symmetric molecules, again induced by

circularly polarized laser pulses.[4,11,12,17] During these studies it was recognized that intramolecular nuclear flux densities appear as uncharted territory of research, calling for the discovery of many new phenomena, irrespective of the specific methods for initiation, e.g., by means of laser pulses.[4,5,7] For example, we have evaluated and analyzed the nuclear flux densities for a 2-dimensional (2D) model of the double proton transfer in porphin[43] — this allowed us to discover an unprecedented switch of the mechanism, from the synchronous forward reaction to the sequential back reaction. Complementary quantum simulations of electronic flux densities accompanying non-adiabatic transitions during classical nuclear motions were pioneered by Takatsuka *et al.*[28–34] and by Patchkovskii.[35] Full quantum evaluations of coherent electronic and nuclear flux densities are still restricted to the simplest system, the vibrating molecular hydrogen ion H_2^+.[13,15,16,18,19] The first experimental results on intramolecular nuclear flux densities have been deduced from ultrafast pump–probe spectra[44,45] only very recently.[9] We are not aware of any experimental observations of intramolecular electronic flux densities, but some concepts are already being developed for this purpose.[46]

This survey presents a selected set of the discoveries on intramolecular nuclear flux densities, with some extensions, which we could make during the years 2012–2014, in pleasant and fruitful cooperation with the partners and coauthors who are quoted in the references, with gratitude.[4–10] All applications are for 1-dimensional (1D) or 3-dimensional (3D) models. This restriction calls for a comment concerning the physical units of flux densities and fluxes. By analogy with the SI units $1/(\mathrm{s}\cdot\mathrm{m}^2)$ of flux densities in 3D (i.e., numbers of particles per time and per area), the SI units of nuclear flux densities in arbitrary n dimensions are $1/\mathrm{s}\cdot\mathrm{m}^{n-1}$. Flux densities of 1D models thus have units of 1/s. Likewise, integrating flux densities over areas in 3D yields the 3D fluxes, with SI units of 1/s. In general, fluxes in arbitrary dimensions have SI units of 1/s. This leads to a special case in 1D where flux densities and fluxes have the same SI units, 1/s. As a consequence, monitoring 1D flux densities is equivalent to measuring fluxes. Due to the integrations of 3D flux densities over 2D surfaces (or over $(n-1)$-dimensional hypersurfaces, for the general n-dimensional case), the resulting fluxes contain in general less detailed information, compared to flux densities, again with the exception of 1D models. Turning

the table, it is in general easier to evaluate fluxes,[13,47–54] or properties which can be derived from fluxes, such as rate constants,[55–66] compared to flux densities, except for the case of 1D models where flux densities and fluxes are identical.

Eventually, we shall also outline how one can initiate the nuclear fluxes, for example by means of a laser pump pulse which induces two photon transitions to an electronic excited state followed by a probe pulse which ionizes the molecule,[44] or by well-designed laser pulses such as single circularly polarized re-optimized π-pulses,[4,17] or by one or even two coherent linearly polarized pump pulses,[7,67] or by an optimal laser pulse which consists of intrapulse pump and dump sub-pulses;[5] the latter[5] as well as the pump–probe spectroscopy[44] imply multi-photon processes, providing a link to the general topic of the present volume of the Advances in Multi-photon Processes and Spectroscopy.

The methods, results and the discussions are presented in Sec. 2, the conclusions are in Sec. 3.

2. Methods, Results and Discussions

The subsequent sections consider nuclear flux densities in 1D (Secs. 2.1–2.3) or 3D (Sec. 2.4) models. The 1D model in Sec. 2.1 actually starts out from a 3D model which is then reduced to 1D, thus supporting the 1D models of Sec. 2.2, and by extrapolation also those of Sec. 2.3. The complementary topics are given in Secs. 2.1–2.4, together with the references for the original discoveries of the phenomena in Ref. 9, Ref. 7, Refs. 5, 6, 8, 10 and Refs. 4, 17, respectively. For each topic, we present an outline of the methods, and the results with discussions. The presentations and the results are analogous, but not identical to the original ones; Secs. 2.3 and 2.4 include also applications to new systems.

2.1. *Experimental results for nuclear flux densities in vibrating Na_2 and D_2^+, deduced from pump–probe spectra*[9]

The first experimental results for intramolecular nuclear flux densities were deduced[9] from pump–probe spectra of a vibrating diatomic molecule and a molecular ion, specifically of Na_2,[44] and D_2^+.[45] The derivation of the nuclear flux densities from the pump–probe spectra proceeds in two steps: First,

the pump–probe spectra are converted into so-called reduced (indicated by tilde ˜, see below) 1D time-dependent nuclear probability densities $\tilde{\rho}_R(R,t)$ depending on the internuclear distance ("radius") R and on time t. In the second step, we employ the 1D continuity equation with proper boundary conditions in order to convert $\tilde{\rho}_R(R,t)$ to the corresponding reduced (1D) radial component $\tilde{j}_R(R,t)$ of the 3D flux density. The two systems, Na_2 and D_2^+, were chosen because at the time of our derivation,[9] these were the only examples for which our experimental colleagues had already succeeded in carrying out the demanding first step;[44,45] a more recent example is documented in Ref. 68. Their methods profited from collecting the pump–probe spectra for molecules with arbitrary orientation angles Θ, Φ. This means that the set of experiments which are considered here (i.e., disregarding refined measurements with angular resolutions[45]) do not account for the 3D probability densities $\rho(R,\Theta,\Phi,t)$ of observing the molecule with bond length R and orientation angles Θ, Φ. Instead, the 3D densities are reduced to 1D densities $\tilde{\rho}_R(R,t)$ such that $d\tilde{P}_R = \tilde{\rho}_R(R,t)dR$ is the probability of observing the diatomic molecule or molecular ion with bond length between R and $R + dR$, irrespective of its orientation. Mathematically, the reduced $\tilde{\rho}_R(R,t)$ are determined by integrating the 3D densities $\rho(R,\Theta,\Phi,t)$ over all molecular orientations (Θ,Φ), and multiplying by R^2

$$\tilde{\rho}_R(R,t) = R^2 \int d\Omega \rho(R,\Theta,\Phi,t). \tag{2.1}$$

In an ideal case, they satisfy the boundary conditions

$$\tilde{\rho}_R(R,t) \to 0 \quad \text{for } R \to 0 \quad \text{and for } R \to \infty \tag{2.2}$$

and the normalization

$$\int_0^\infty dR\tilde{\rho}_R(R,t) = \int_0^\infty dR R^2 \int d\Omega \rho(R,\Theta,\Phi,t) = 1. \tag{2.3}$$

The experimental strategies and details for determining $\tilde{\rho}_R(R,t)$ depend on the systems, see Refs. 44, 69, 70 and Refs. 45, 71, 72 and Ref. 68 for the examples, Na_2, D_2^+ and Br_2, respectively. The subsequent presentation will center attention on application to Na_2. Thus suffice it here to say that in the case of the Na_2 molecule, the ultrashort (full widths at half maximum is 40 fs), weak (intensity is $\sim 10^{11}$ W/cm^2), linearly (Z-) polarized pump pulse

achieves a two-photon transition from the $X^1\Sigma_g^+$ electronic ground via the $A^1\Sigma_u^+$ to the $2^1\Pi_g$ excited state. At the same time, the radial nuclear wave function is lifted from the vibrational ground state (which is embedded in the potential energy curve of the electronic ground state $X^1\Sigma_g^+$) in a vertical, Franck–Condon (FC) type manner to the inner turning point of the potential curve of the $2^1\Pi_g$ excited state. Subsequently, the electronic excited nuclear wave function vibrates essentially between the corresponding inner and outer turning points of the potential of the $2^1\Pi_g$ state. On the way, the probe pulse ionizes the system from the $2^1\Pi_g$ state of the neutral Na_2 to the electronic ground state $^2\Sigma_g^+$ of the molecular sodium ion, Na_2^+. The experimental observable is the distribution of kinetic energies $K(t)$ of the excess electrons after ionization, depending on the time delay t (and various other properties such as the carrier frequency ω) between the pump and probe pulses. The distribution of $K(t)$ in turn depends on the distribution of the bond lengths R at the time t of ionization. Ultimately, the experimental signals $K(t)$ can thus be converted to the nuclear densities $\tilde{\rho}_R(R,t)$ in the electronic excited state.[44]

Exemplarily, we consider the pump–probe signals, and hence also the reduced densities $\tilde{\rho}_R(R,t)$, for just a rather small window of delay times t which is chosen such that the two pump and probe laser pulses do not overlap. Moreover, for practical experimental reasons, the observations of sufficiently well-resolved pump–probe signals may be restricted to an accessible domain of the distributions of kinetic energies, say $K_{\min} < K(t) < K_{\max}$. This may result in the corresponding restriction of the accessible radial domain of the nuclear densities, say $R_{\min} < R < R_{\max}$. Usually, this radial domain is large enough such that the condition (2.2) is satisfied. Else we have imposed that boundary condition by extrapolation of the experimental $\tilde{\rho}_R(R,t)$, assuming exponential decay in the domains beyond $[R_{\min}, R_{\max}]$. Moreover, we have imposed the normalization (2.3) by re-normalization of the experimental densities, with proper observation of the boundary conditions (2.2). This corresponds to the ideal scenario of 100% preparation of the molecule in the excited electronic target state, i.e., $Na_2(2^1\Pi_g)$. Else if the real preparation yields a smaller probability of finding the system in the excited (e) state after the laser pulse, $P_e < 1$, then the resulting nuclear densities and flux densities are also diminished by the same factor P_e.

The second step, that means the conversion of the reduced 1D radial nuclear density $\tilde{\rho}_R(R,t)$ to the corresponding reduced 1D radial component of the nuclear flux density $\tilde{j}_R(R,t)$, starts from the 3D continuity equation for the non-reduced nuclear density and the radial (R) as well as two angular (Θ, Φ) components of the nuclear flux density[73]

$$\begin{aligned}\frac{\partial}{\partial t}\rho(R,\Theta,\Phi,t) &+ \frac{1}{R^2}\frac{\partial}{\partial R}R^2 j_R(R,\Theta,\Phi,t)\\ &+ \frac{1}{R\sin(\Theta)}\frac{\partial}{\partial\Theta}\sin(\Theta)j_\Theta(R,\Theta,\Phi,t)\\ &+ \frac{1}{R\sin(\Theta)}\frac{\partial}{\partial\Phi}j_\Phi(R,\Theta,\Phi,t) = 0. \end{aligned} \tag{2.4}$$

The linear (Z) polarization of the pump pulse implies that it does not induce any nuclear rotations about the Z-axis (in contrast with circularly polarized laser pulses[4,11,12,17]), hence the component $j_\Phi(R,\Theta,\Phi,t)$ is equal to zero. Next, by analogy with the reduction of the density (2.1), we integrate the 3D continuity equation (2.4) over the solid angles and multiply by R^2, thus

$$\begin{aligned}\frac{\partial}{\partial t}R^2\int d\Omega\rho(R,\Theta,\Phi,t) &+ \frac{\partial}{\partial R}\int d\Omega R^2 j_R(R,\Theta,\Phi,t)\\ &+ R\int d\Omega\frac{1}{\sin(\Theta)}\frac{\partial}{\partial\Theta}\sin(\Theta)j_\Theta(R,\Theta,\Phi,t)\\ &= \frac{\partial}{\partial t}\tilde{\rho}_R(R,t) + \frac{\partial}{\partial R}\tilde{j}_R(R,t) = 0. \end{aligned} \tag{2.5}$$

For the first term of Eq. (2.5), we have used the definition (2.1). By analogy, for the second term we define the reduced (1D) radial flux density

$$\tilde{j}_R(R,t) = R^2\int d\Omega j_R(R,\Theta,\Phi,t) \tag{2.6}$$

which accounts for the (differential numbers of) diatomic molecule that vibrate or "flow" to the bond distance R per (differential) time, with boundary conditions

$$\tilde{j}_R(R,t) \to 0 \quad \text{for } R \to 0 \quad \text{and} \quad R \to \infty. \tag{2.7}$$

The third term of Eq. (2.5) vanishes on reduction from 3D to 1D because the product term $\sin(\Theta) j_\Theta(R, \Theta, \Phi, t)$ of the integrand vanishes at the integration boundaries, $\Theta = 0$ and π.

The second part of Eq. (2.5) takes the form of the 1D continuity equation for the reduced density $\tilde{\rho}_R(R, t)$ and flux density $\tilde{j}_R(R, t)$. Together with the boundary condition (2.7) it allows to convert $\tilde{\rho}_R(R, t)$ into[9]

$$\tilde{j}_R(R, t) = -\frac{\partial}{\partial t} \int_0^R dR' \tilde{\rho}_R(R', t). \tag{2.8}$$

Exemplary results of this conversion of the (re-normalized) experimental reduced density $\tilde{\rho}_R(R, t)$ (adapted from Ref. 44) to the reduced flux density $\tilde{j}_R(R, t)$ (adapted from Ref. 9) are shown in panels a and b of Fig. 1, respectively, for the case of the vibrating Na_2 molecule in the electronic excited $2^1\Pi_g$ state. Apparently, the oscillatory pattern of $\tilde{\rho}_R(R, t)$ corresponds to approximately two vibrational round trips during the chosen time window from 1000 to 1800 fs, each one from short to long and back to short internuclear bond lengths. The corresponding patterns of the nuclear flux densities oscillate between positive and negative values representing the related alternating bond stretches and compressions, respectively. Figures 1(c) and 1(d) show a blow-up of the reduced densities and flux densities from 1274.0 till 1473.8 fs, focusing on the turn from compression to bond stretch. The result for $\tilde{j}_R(R, t = 1407.2\,\text{fs})$ reveals a fascinating quantum effect which we call the "quantum accordion"[9]; for an illustration, see Fig. 1(e). For reference, in a classical (idealized, 1D) accordion, there is a moment in which all the bellows remain still as the pull turns to push. This instant would correspond to the classical result $\tilde{j}_{\text{cl}}(R, t) = 0$. In contrast, the quantum mechanical $\tilde{j}_R(R, t)$ never vanishes completely. Instead, for example at $t = 1407.2$ fs, it has small absolute values (compared to the maximum ones), with negative signs in the domains of small and large values of R, separated by an intermediate domain with positive signs. The corresponding bellows of the "quantum accordion" thus expand and contract in opposite directions — they never stand still altogether. The "quantum accordion" was discovered together with three additional quantum effects.[9] In general, the flux densities $\tilde{j}_R(R, t)$ lend themselves more easily to the discovery of these types of time-dependent quantum effects than the probability densities $\tilde{\rho}_R(R, t)$.

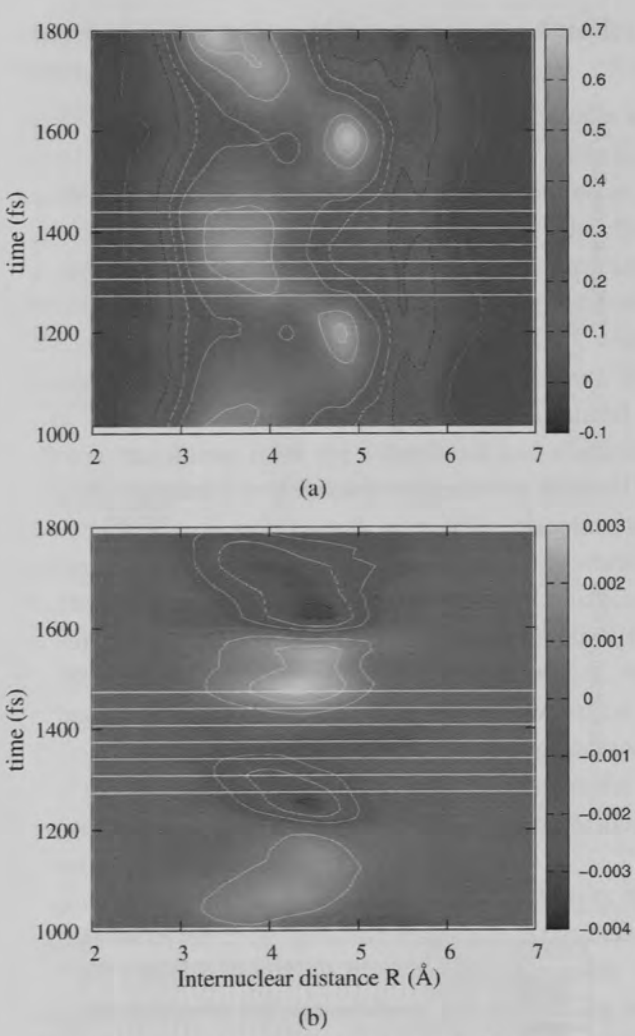

Fig. 1. Reduced 1D radial nuclear densities $\tilde{\rho}_R$ (in units of Å^{-1}; panels a, c, adapted from Ref. 9) and flux densities $\tilde{j}_R$ (in units of $10^{-2}\,\text{fs}^{-1}$; panels b, d, adapted from Ref. 9) of Na_2 vibrating in the electronic excited $2^1\Pi_g$ state. The times for the snapshots shown in panels c, d are indicated by horizontal lines in panels a, b. Panel e: cartoon of the "quantum accordion" with various bellows moving towards opposite directions, illustrating the quantum effect at $t = 1407.2\,\text{fs}$ with various parts of the nuclear flux densities moving towards opposite directions (adapted from Ref. 9, courtesy of F. Korinth, FU Berlin). For figure in full color, refer to Appendix (Page 226).

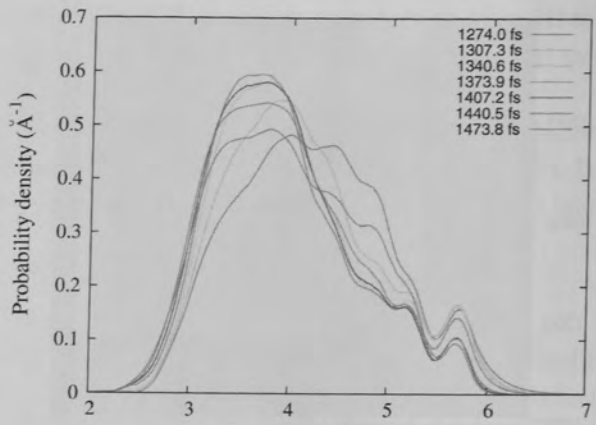

(c)

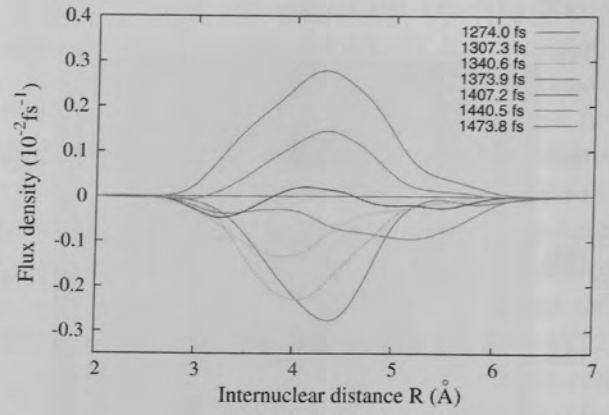

(d)

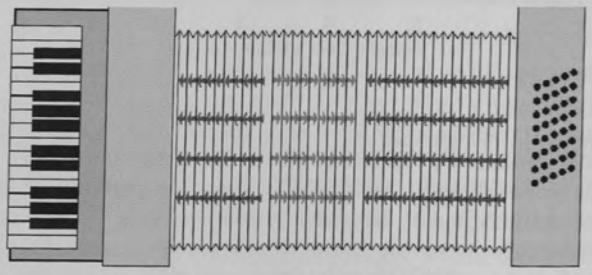

(e)

Fig. 1. (*Continued*)

2.2. *Quantum model simulations of the nuclear flux densities in vibrating I_2[7] and H_2^+*

The purpose of this section is to present two quantum model simulations of the reduced (1D) nuclear flux densities in a vibrating diatomic molecule and in a diatomic molecular ion, which may be considered as somewhat analogous to the experimental results of Sec. 2.1. The two specific applications are for the vibrating I_2 molecule in the electronic excited state B (labeled $e = 1$ below), using the model (adapted from Ref. 67) and extending part of the results of Ref. 7, and for the H_2^+ molecular ion in the electronic ground state $^2\Sigma_g^+$ (labeled $e = 1$ below). Both model simulations are for scenarios where the vibrations are initiated essentially by single photon transitions from the vibrational and electronic ground states of I_2 and H_2 (labeled $e = 0$ below), respectively, induced by linearly polarized laser pulses with rather weak intensities; quantum simulations of the experimental reduced 1D nuclear flux densities in vibrating Na_2,[44] or D_2^+,[45] which are initiated by two- or multi-photon transitions from the electronic ground states of Na_2 and D_2 at low temperatures, induced by linearly polarized laser pulses with weak and strong intensities, respectively, have not yet been carried out. The quantum model simulation for I_2 will be presented first, followed by that for H_2^+. We keep the nomenclature and presentation of the methods general so that they are also useful for the 1D and 3D models of nuclear flux densities in polyatomic molecules which are presented in Secs. 2.3 and 2.4, respectively.

The present model simulation of the nuclear flux density in vibrating I_2(B) is an extension of the corresponding result which has been presented in Ref. 7, for the case of excitation by a single laser pulse. Additional results for excitations by two coherent laser pulses causing wavepacket interferometry of nuclear flux densities have also been reported,[7,67] but these will not be demonstrated below. In the non-relativistic limit, the time evolution of the laser driven system is then simulated in terms of wave functions

$$\Psi(\mathbf{r}, R, t) = \sum_e \Phi_e(\mathbf{r}; R)\Psi_e(R, t), \tag{2.9}$$

where $\Phi_e(\mathbf{r}; R)$ are the Born–Oppenheimer (BO) electronic energy eigenfunctions depending on all electronic degrees of freedom $\mathbf{r}$ and depending

parametrically on the bond length R; these are associated the potential energy curves $V_e(R)$. In Sec. 2.3, the nuclear coordinate R will be replaced by a more general nuclear "reaction coordinate" Q, and $V_e(Q)$ will serve as 1D-cuts of the multi-dimensional (multi-D) potential energy surfaces (PESs). In general, we employ small ($\mathbf{r}$) and capital (R, Q) letters for electronic and nuclear degrees of freedom, respectively. Electronic and nuclear spins are not denoted explicitly, but they are omni-present implicitly, e.g., they impose proper antisymmetrizations of the electronic wave functions as well as antisymmetrizations/symmetrizations of the nuclear wave functions representing sets of equivalent nuclei with half integer and integer nuclear spins, respectively.

The sum in Eq. (2.9) is over all relevant electronic states e; in the present application to I_2, we consider an electronic two-state model, thus $e = 0$ and 1. Sections. 2.3 and 2.4 shall focus exclusively on nuclear flux density in the electronic ground state, thus $e = 0$. In general, both $\Phi_e(\mathbf{r}; R)$ and $V_e(R)$ are obtained as solutions of the time-independent electronic Schrödinger equation at fixed internuclear distance R or, in general, at fixed values of the nuclear coordinates. The $\Psi_e(R, t)$ are the associated nuclear wave functions in electronic states e, depending on R and time t. The exclusive dependence on R (and not on the orientation angles Θ, Φ) corresponds to the 3D to 1D reduction which has been outlined in Sec. 2.1. Alternatively, the reduced 1D model may also be used for approximate simulations of laser driven diatomic molecules or molecular ions which are aligned or oriented along a preferential (typically the Z-) direction in the laboratory. The $\Psi_e(R, t)$ then satisfy the corresponding 1D time-dependent nuclear Schrödinger equation (TDNSE). Neglecting the kinetic coupling terms and using the semiclassical dipole approximations, the TDNSE is written in matrix form as

$$i\hbar\frac{\partial}{\partial t}\begin{pmatrix}\Psi_1\\ \Psi_0\end{pmatrix} = \begin{pmatrix}T+V_1 & 0\\ 0 & T+V_0\end{pmatrix}\begin{pmatrix}\Psi_1\\ \Psi_0\end{pmatrix} - \mathcal{E}(t)\cdot\begin{pmatrix}0 & d_{10}\\ d_{01} & 0\end{pmatrix}\begin{pmatrix}\Psi_1\\ \Psi_0\end{pmatrix}, \tag{2.10}$$

where $T = P^2/2\mu$ is the kinetic energy operator with momentum operator $P = -i\hbar\partial/\partial R$ and reduced mass μ; for homonuclear diatomic molecules, $\mu = M/2$ where M is the mass of the individual nuclei; for iodine, we employ the value $M = 127\,\mathrm{u}$ (in atomic mass units u). The potential curves

$V_0(R) = V_X(R)$ and $V_1(R) = V_B(R)$ are adapted from Refs. 74 and 75, respectively, as in Refs. 7, 67. Laser induced transitions between states $e = 0$ and 1 are mediated by the transition dipole operators $d_{01} = d_{10} = d$ which interact with the electric field

$$\mathcal{E}(t) = \mathcal{E}_0 s(t) \cos(\omega t) \tag{2.11}$$

with amplitude $\mathcal{E}_0$ and Gaussian shape function

$$s(t) = \exp\left[-\frac{(t - t_0)^2}{2\tau^2}\right], \tag{2.12}$$

centered at time t_0. The laser parameters are chosen such that in Condon approximation, $\mathcal{E}_0 \cdot d = 0.0327$ eV, corresponding to $P_e = 0.011$ population transfer from states $e = 0$ to 1 at the end of the laser pulse, which is centered at $t_0 = 300$ fs; its duration is determined by setting $\tau = 100$ fs; the values of the carrier frequency ω corresponds to the photon energy $\hbar\omega = 2.087$ eV — this is slightly below the energy for resonant Franck–Condon transition, in order to generate pure vibrations of I_2 in the excited B-state ($e = 1$), without any competing photodissociations. In other systems that means in heteronuclear diatomic or in polyatomic molecules, the laser pulse (2.11) may also interact with the non-zero elements of the molecular dipole operators $d_e(R)$ or $d_e(Q)$ in electronic states e, respectively, calling for the corresponding additional terms $-d_e(R) \cdot \mathcal{E}(t)$ or $-d_e(Q) \cdot \mathcal{E}(t)$ in Eq. (2.10).

The TDNSE (2.10) is solved by means of standard techniques as specified in Ref. 7. The propagation starts from the initial wave function

$$\begin{pmatrix} \Psi_1(R, t = 0) \\ \Psi_0(R, t = 0) \end{pmatrix} = \begin{pmatrix} 0 \\ \chi_{00}(R) \end{pmatrix}, \tag{2.13}$$

where $\chi_{00}(R)$ represents the vibrational ground state in the electronic ground state, adapted from Ref. 7. The quantities of present interest are the resulting nuclear densities

$$\rho_e(R, t) = |\Psi_e(R, t)|^2, \quad e = 0, 1 \tag{2.14}$$

and the nuclear flux density

$$j_e(R, t) = \frac{1}{2}\left(\Psi_e^*(R, t)\frac{P}{\mu}\Psi_e(R, t) - \Psi_e(R, t)\frac{P}{\mu}\Psi_e^*(R, t)\right) \tag{2.15}$$

in the electronic excited state, $e = 1$. These are evaluated numerically as outlined in Ref. 7.

After the laser pulse, one may scale $\rho_{e=1}(R,t)$ and $j_{e=1}(R,t)$ by the same normalization factor $1/P_{e=1}$ such that

$$\tilde{\rho}_R(R,t) = \rho_e(R,t)/P_e, \tag{2.16}$$

$$\tilde{j}_R(R,t) = j_e(R,t)/P_e. \tag{2.17}$$

The resulting reduced densities $\tilde{\rho}_R(R,t)$ of the vibrating I_2(B) confirm a well-known phenomenon, i.e., the laser pulse induces quasi-periodic sequences of three phases of the vibrational quantum dynamics: (i) vibrational round trips that correspond to classical motion, (ii) quantum dispersion of the wavepacket, and (iii) vibrational revivals.[76,77] The initial phase (i) during the time window from 0 till 2.5 ps has already been analyzed in Ref. 7, for similar choices of the laser parameters. Here we document results for $\tilde{\rho}_R$ (cf. Fig. 2(a)) and, for the first time, also for $\tilde{j}_R(R,t)$ (Fig. 2(b)) during the time window from 18 till 40 ps, comprising the complete sequence of all three phases (i)–(iii). Four horizontal lines in Figs. 2(a) and 2(b) are drawn for the times t(i) = 18.400 ps, t(ii) = 27.933 and 28.004 ps and t(iii) = 37.460 ps of some characteristic phenomena during phases (i), (ii) and (iii), respectively. The corresponding snapshots of $\tilde{\rho}_R(R,t)$ and $\tilde{j}_R(R,t)$, embedded in the potential curve $V_1(R)$ of the excited B-state of the I_2 molecule, are documented in Figs. 2(c)–2(f), respectively. Apparently, at t(i) = 18.4 ps, the wave function turns from bond compression to expansion. The head and the tail of the wave function thus run into opposite directions, causing interferences which result in "quantum ripples" of the (reduced) density $\tilde{\rho}_R(R,t)$ and corresponding changes of the signs of the nuclear flux density $\tilde{j}_R(R,t)$. At t(ii) = 27.933 and 28.004 ps, the wave function is dispersed over the entire domain between the classical turning points. The corresponding snapshots for the nuclear flux density $\tilde{j}_R(R,t)$ reveal that essentially, this is a consequence of interferences of two partial waves which run in opposite directions, either towards, or away from the two classical turning points. At $t = 27.933$ ps, these interferences cause multiple changes of signs in $\tilde{j}_R$. This effect for the pure quantum state at zero temperature reminds of the experimental results[44] for the "quantum accordion" at finite temperature, as discovered

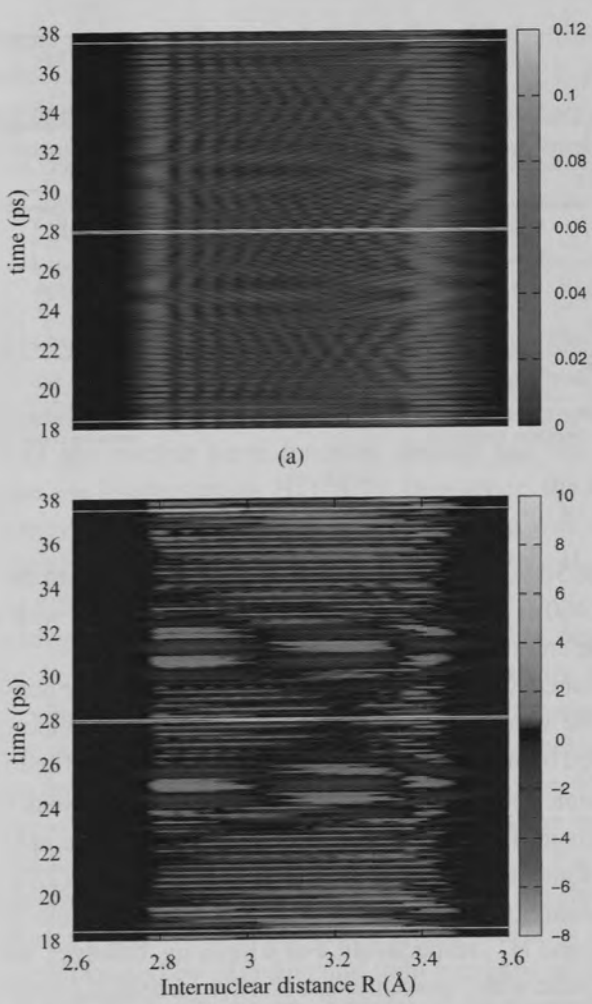

Fig. 2. Reduced 1D radial nuclear densities $\tilde{\rho}_R$ (in units of Å^{-1}; panels a, c–f) and flux densities $\tilde{j}_R$ (in units of $10^{-5}\,\text{ps}^{-1}$; panels b–f) of I_2 vibrating in the electronic excited B-state. The times for the snapshots shown in panels c–f are indicated by horizontal lines in panels a, b. The snapshots show $\tilde{\rho}_R$ and $\tilde{j}_R$ embedded in the potential energy curve $V_B(R)$ of the B-state, adapted from Refs. 7, 75, in the energetic domain from the potential minimum at 0.0714 E_h to 0.095 E_h. The baseline of $\tilde{\rho}_R$ and $\tilde{j}_R$ corresponds to the mean energy of the wavepacket, $E = 0.0775\ E_h$. For figure in full color, refer to Appendix (Page 228).

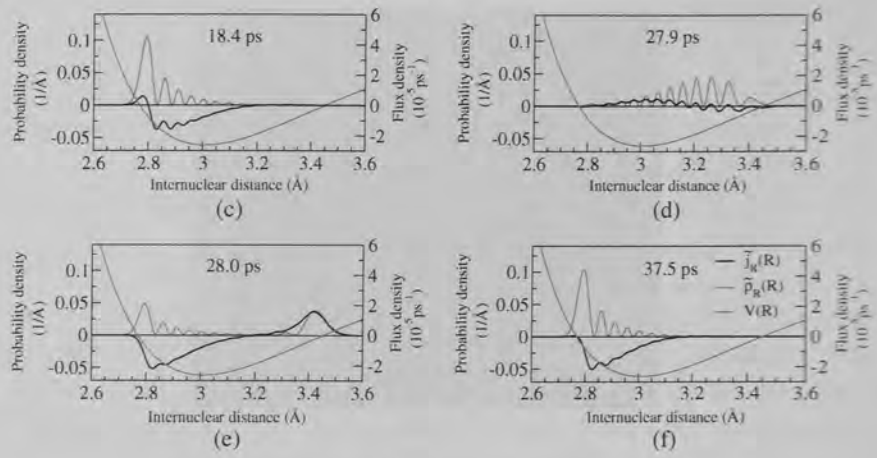

Fig. 2. (*Continued*)

in Ref. 9, see Sec. 2.1. Finally, the phenomena illustrated in the snapshot at $t(\text{iii}) = 37.460\,\text{ps}$ are similar to those for $t(\text{i})$, in accord with wavepacket revival at the end of the events (i)–(iii).

The second example is for the reduced (1D) nuclear density and flux density of the vibrating molecular ion H_2^+ in the electronic ground state $^2\Sigma_g^+$, initiated by ultrafast single photon ionization of the neutral molecule in the electronic and vibrational ground state $^1\Sigma_g^+$, in the weak field limit. In principle, this initiation may be modeled by means of the approach which has been outlined for the previous example (I_2), see Eqs. (2.9)–(2.17), now with new meanings of the electronic states $e = 0$ and 1 as electronic ground states of H_2 and H_2^+, respectively. For simplicity, however, we replace the pump laser pulse with Gaussian shape (2.12) by a delta pulse which transfers the vibrational ground state $\chi_{00}(R)$ of H_2 by a quasi-instantaneous FC-type vertical transition from state $e = 0$ of H_2 to $e = 1$ of H_2^+, with small probability P_1 of the population transfer. It turns out that this initiation would induce not only vibrations of H_2^+, but also dissociation $\rightarrow H + H^+$, with probabilities P_{vib} and P_{dis}, respectively. Accordingly, after FC-type preparation of the (normalized) nuclear wavepacket $\chi_{00}(R)/\sqrt{P_1}$ in the electronic ground state of the H_2^+ ion, it consists of two orthogonal partial waves, with energies below and above the threshold for photodissociation,

$$\chi_{00}(R)/\sqrt{P_1} = \chi_{00,\text{vib}}(R)/\sqrt{P_1} + \chi_{00,\text{dis}}(R)/\sqrt{P_1}. \tag{2.18}$$

For the present purpose, i.e., model simulations of the (reduced, 1D) nuclear density and flux density of the vibrating $H_2^+(^2\Sigma_g^+)$, we suppress the dissociative partial wave and renormalize the remaining vibrational part, i.e., we propagate Eq. (2.10) starting from the initial wave function,

$$\begin{pmatrix} \Psi_1(R, t=0) \\ \Psi_0(R, t=0) \end{pmatrix} = \begin{pmatrix} \chi_{00,\mathrm{vib}}(R)/\sqrt{P_1 P_{\mathrm{vib}}} \\ 0 \end{pmatrix}, \tag{2.19}$$

where $t = 0$ is now defined as the time immediately after the delta pulse. Numerically, we can ignore the history of the preparation of H_2^+ in the electronic ground state, that, means we can restrict the propagation and the analyses of the nuclear wave function, density and flux density to the single state $e = 1$ representing $H_2^+(^2\Sigma_g^+)$. In practice, the dissociative partial wave may be suppressed by using a laser pulse with one-photon energy sufficiently below the resonance energy for FC-type $H_2 \rightarrow H_2^+ + e$ photoionization.

The resulting reduced (1D) nuclear density and flux density of the $H_2^+(^2\Sigma_g^+)$ ion are shown in Figs. 3(a) and 3(b), respectively. Apparently, they describe vibrational round trips from the inner to the outer classical turning points at small and large bond lengths R, respectively; these turning points are defined by $V(R) = E$ where $V(R) = V_1(R)$ is the potential curve of $H_2^+(^2\Sigma_g^+)$, and $E = -0.5666\ E_h$ is the mean energy of the wavepacket. The potential $V(R)$ is illustrated in Fig. 3(e). The corresponding vibrational period is $\tau = 17.5$ fs, close to the classical limit. The much shorter period of vibration documented in Ref. 9 is a strong-field phenomenon caused by experimental field strengths of the order of 10^{15} W/cm^2 in Ref. 45. Some important details of the quantum dynamics are discovered by the snapshots shown in Figs. 3(c)–3(e). Accordingly, closely before the end of the first round trip at 15 fs, the wavepacket returns to the FC-domain close to the inner turning point. Subsequently, we observe quantum effects similar to those shown in Figs. 1(c)–1(e) for $Na_2(2^1\Pi_g)$, i.e., the "head" of the wavepacket is already reflected from the steep repulsive wall of the potential curve, while the "tail" of the wavepacket is still running towards the inner turning point, causing interferences of the "head" and "tail" parts of the wavepacket until it is reflected completely. The interferences are not only visible in the nuclear densities (Fig. 3(c))

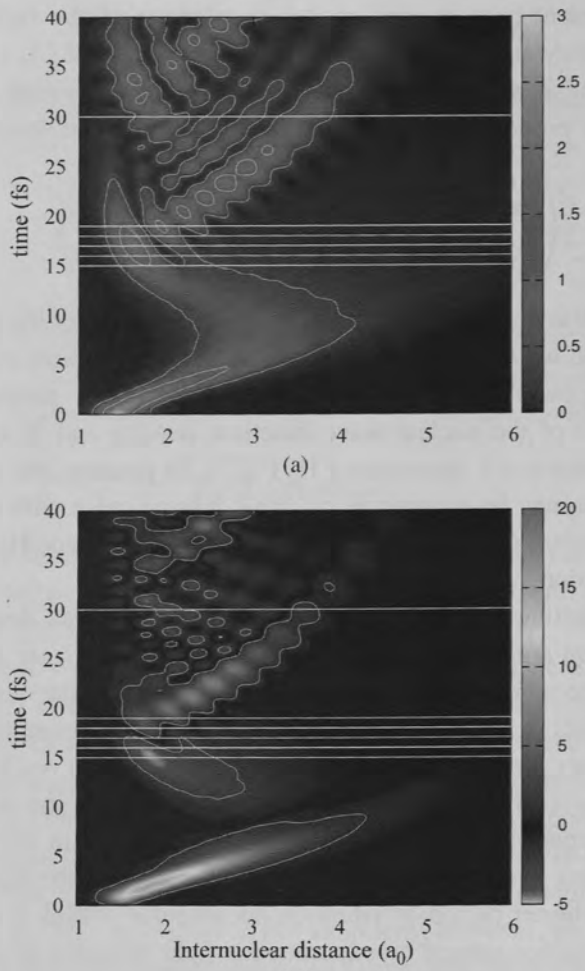

Fig. 3. Reduced 1D radial nuclear densities $\tilde{\rho}_R$ (in units of a_0^{-1}; panels a, c, e) and flux densities $\tilde{j}_R$ (in units of $10^{-3}\ E_h/\hbar$; panels b, d, e) of H_2^+ vibrating in the electronic ground state $^2\Sigma_g^+$. The times for the snapshots shown in panels c, d, e are indicated by horizontal lines in the contour plots of panels a, b. The snapshots in panel e show the reduced density and the reduced flux density embedded in the potential curve V_1 of the electronic ground state of H_2^+, with energetic domain from the potential minimum at $-0.6026\ E_h$ to $-0.4514\ E_h$, and with the base line at the value $-0.5666\ E_h$ of the mean energy. For figure in full color, refer to Appendix (Page 230).

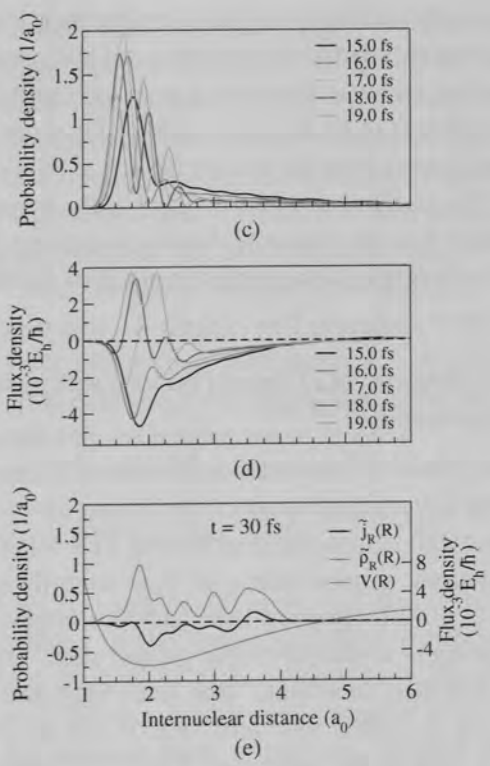

Fig. 3. (*Continued*)

but also in the flux densities (Fig. 3(d)). As a consequence, the nuclear flux densities at 17 fs and at 18 fs display two or even four changes of sign, thus exhibiting the effect of the "quantum accordion", cf. Fig. 1(e). As for the results for Na_2 documented in Sec. 2.1, this quantum effect is discovered much more easily by means of the flux densities, compared to the densities. Subsequently, the much lighter mass of H_2^+ compared to Na_2 (Sec. 2.1) or I_2 (first part of the present section) causes much more rapid dispersion of the wavepacket of H_2^+, compared to the heavier diatomic molecules. As a consequence, already during the second vibrational round trip of H_2^+, the wavepacket spreads over the entire domain from the inner to the outer turning point. This is illustrated in Fig. 3(e), by the snap shot at 30 fs close to the end of the second round trip: the "head" of the wave function is already approaching the inner turning point while its "tail" is still

on the way to the outer turning point. As a consequence, the wave function starts to separate into two partial waves which run into opposite directions. Again, this quantum effect is discovered more efficiently by analysis of the nuclear flux density (which at 30 fs consists of two parts with opposite signs, cf. Fig. 3(e)) rather than the density (which at 30 fs spreads over the entire domain). The mechanism of the division of the wavepacket into two partial waves which flow into opposite directions explains the origin of the phenomena which have been documented in Fig. 2(d), for the case of I_2(B).

2.3. *Nuclear flux densities in 1D model systems with symmetric double-well potentials*[5,6,8,10]

In this section, we extend the presentation of reduced 1D nuclear flux densities from vibrating diatomic molecules or molecular ions to isomerizations of model systems with symmetric double-well PES $V(Q) = V(-Q) = V_0(Q)$ in the electronic ground state $e = 0$; to simplify the notation, the electronic label $e = 0$ is dropped here and also below, whenever it is clear that the system is in the electronic ground state. The coordinate Q denotes the 1D "reaction coordinate" that leads from one of the potential minima, $V(Q_l) = 0$ (called the "left" one, l) via the potential barrier $V(0) = B$ at $Q = 0$ to the other one, $V(Q_r) = 0$ (called the "right" one, r; $Q_r = -Q_l \equiv Q_0$). The corresponding molecular configurations close to Q_l and Q_r are called reactant (R) and product (P), respectively. The original investigations of nuclear flux densities during these types of reactions[5,6,8,10] were stimulated, in part, by the discovery of an effect of the energy on electronic fluxes during isomerizations of a model system which is supported by a symmetric double-well potential. Specifically, for the example of the Cope rearrangement of semibullvalene (SBV) it was shown that for energies above ($E > B$) and below ($E < B$) the potential barrier B, the electronic fluxes which accompany bond breaking in the reactant R and bond formation in the product P flow asynchronously and synchronously, respectively,[51] see also Refs. 50, 78. This suggested to search for differences of the related nuclear fluxes during this or analogous types of isomerizations with $E > B$ compared to $E < B$. Ultimately, this motivation led to the discovery of several, possibly even counterintuitive phenomena of reduced nuclear fluxes during reactions from R to P along

Q, in symmetric double-well potentials $V(Q)$.[6,8,10] Here we present some of these phenomena, with application to two 1D model systems, e.g., for inversion of per-deuterated ammonia ND_3. We are aware of the fact that it is now possible to describe these types of "reactions" from R to P using sophisticated multi-D models, for the case of the inversion of ammonia.[79–81] The results for the present simple 1D models should stimulate searches for related phenomena of nuclear flux densities in the multi-D systems.

Below, we shall consider nuclear flux densities during model "reactions" in symmetric 1D double-well potentials $V(Q)$, from R along coordinate Q to P, first for the case with energy $E > B$, second for the other case where $E < B$. In both cases, we assume that in the very beginning, the system is represented by the reactant wave function

$$\Psi_R(Q) = \frac{1}{\sqrt{2}}[\Psi_0(Q) + \Psi_1(Q)], \tag{2.20}$$

where $\Psi_0(Q) \equiv \Psi_+(Q)$ and $\Psi_1(Q) \equiv \Psi_-(Q)$ denote the wave functions with $+$ and $-$ parities of the lowest so-called tunneling doublets with eigenenergies $E_0 = E_+$ and $E_1 = E_-$, respectively. For chiral molecules, the reactant state (2.20) in a double-well potential is a pure enantiomer state that can be obtained from a racemate ground state $\Psi_0(Q)$ by means of a sequence of optimized linearly alternated x- and y-[82–88] or circularly[89] polarized laser pulses. Stochastic laser pulse optimization for such enantioselective control can also be used, see the applications to the more demanding three-well potential containing two chiral and one achiral molecular configurations.[90,91] The wave functions $\Psi_0(Q)$ and $\Psi_1(Q)$ are obtained as solutions of the time-independent nuclear Schrödinger equation

$$H\Psi_n(Q) = \left[\frac{P_Q^2}{2\mu} + V(Q)\right]\Psi_n(Q) = E_n\Psi_n(Q), \tag{2.21}$$

where $P_Q = -i\hbar\partial/\partial Q$ denotes the momentum operator conjugate to Q, and μ is the corresponding reduced mass. Likewise, we define the product wave function

$$\Psi_P(Q) = \frac{1}{\sqrt{2}}[\Psi_0(Q) - \Psi_1(Q)]. \tag{2.22}$$

For example, for the case of the inversion of the "umbrella" of the three ND bonds of ND_3 in C_{3v} symmetry, Q is approximately the distance from the nucleus of the nitrogen atom to the center of mass of the three deuterium atoms; the related reduced mass is $\mu = m_N \times 3m_D/(m_N + 3m_D)$. The resulting wave functions $\Psi_R(Q), \Psi_P(Q)$ are shown in the top panel of Fig. 4(b), embedded in the 1D PES which is adapted from Ref. 92. Its potential minima are located at $Q_r = -Q_l = 0.207\,\text{Å}$, the barrier height is $B = 0.250\,\text{eV}$. The resulting mean value of the eigenenergies

$$\bar{E} = 0.5(E_0 + E_1) = 0.050\,\text{eV} \approx E_{\text{ZPE}} \tag{2.23}$$

serves as zero point energy (ZPE) of the R and P configurations.

Isomerizations with $E > B$ may be induced by means of two pump and dump laser pulses, or by intrapulse two-photon transitions which induce corresponding pump and dump processes:[5] Essentially, the pump pulse transfers the nuclear wave function $\Psi_R(Q)$ representing R by means of a nearly vertical FC-type transition from the electronic ground state $e = 0$ to an excited state, $e = 1$, similar to the effect of the pump pulses which have been employed in Secs. 2.1 and 2.2 for excitations or ionizations of diatomic molecules. There it evolves on the PES $V_{e=1}$ of the excited state. Under favorable conditions, that means in case of a steep gradient of V_1 directed from R to P, the nuclear wavepacket is accelerated, gaining translational energy $\langle T \rangle$ with momentum directed from R to P. Soon after the pump pulse when the nuclear wavepacket is still in the domain of the reactant well (that means $\langle Q \rangle \sim Q_l$, where $\langle Q \rangle$ denotes the mean value of Q), without any significant dispersion but with sufficiently high value of $\langle T \rangle$ such that the sum $\langle T \rangle + V(\langle Q \rangle)$ is already above the barrier B, the dump pulse induces another nearly vertical FC-type transition, this time from the electronic excited state $e = 1$ back to the ground state, conserving not only nuclear positions but also the momenta and the kinetic energy $\langle T \rangle$. This way, the nuclear wavepacket is prepared with shape close to the $\Psi_R(0)$, but with momentum $\hbar k \approx \sqrt{2\mu\langle T \rangle}$. Experimentally, this type of initiation of isomerization reactions from R to P has been pioneered by Iwakura, Kobayashi and coworkers.[93,94] The first "reduced" 1D model simulation was demonstrated with application to the Cope rearrangement of SBV.[5] The methods used in Ref. 5 were essentially the same as those described in Sec. 2.2, except that the pump and dump laser pulses were obtained as

sub-pulses of an optimal laser pulse, designed by means of the methods for optimal control.[95–99] In the present model simulation of the inversion of ND_3, we will not repeat this design of the laser pulse explicitly but simply assume that at the "initial" time $t = 0$ (now re-defined as the time immediately after the pump and dump laser pulses) the initial wave function is prepared approximately as

$$\Psi(Q, t = 0) \approx \Psi_R(Q) \exp(ikQ) \tag{2.24}$$

with total energy

$$E \approx E_{\mathrm{ZPE}} + \frac{(\hbar k)^2}{2\mu} > B. \tag{2.25}$$

Note that the initial density is equal to the density of the reactant wave function,

$$\rho(Q, t = 0) = |\Psi(Q, t = 0)|^2 = |\Psi_R(Q)|^2 = \rho_R(Q). \tag{2.26}$$

For our application to ND_3 we set $E = 0.580\,\mathrm{eV}$ thus $E > B$. The time evolution of the wave function $\Psi(Q, t)$ starting from the initial wave function (2.24) is then evaluated as solution of the TDNSE

$$i\hbar \frac{\partial}{\partial t} \Psi(Q, t) = H \Psi(Q, t) \tag{2.27}$$

together with the resulting (reduced, 1D) nuclear densities $\rho(Q, t)$ and flux densities $j(Q, t)$. The methods are essentially the same as those used in Sec. 2.2, except that the previous equations are now restricted (that means simplified) to the electronic ground state, $e = 0$. For simplicity of the notation, we omit the tilde "~" for the reduced density and flux density, for the rest of this section.

The resulting reduced nuclear density $\rho(Q, t)$ and flux density $j(Q, t)$ from time $t = 0$ to τ_r are shown in Fig. 4(a), by means of snapshots (top panel) and by contour plots for equi-densities (second from top panel) and equi-flux densities (third from top panel). Here the "reaction time τ_r" is defined as the time when the nuclear density $\rho(Q, t = \tau_r)$ has maximum overlap with the product density $\rho_P(Q) = |\Psi_P(Q)|^2$, $\tau_r = 19.3\,\mathrm{fs}$. Apparently, the quantum mechanical density $\rho(Q, t)$ evolves along the corresponding classical (cl) trajectory $Q_{cl}(t)$ from R along Q to P. The

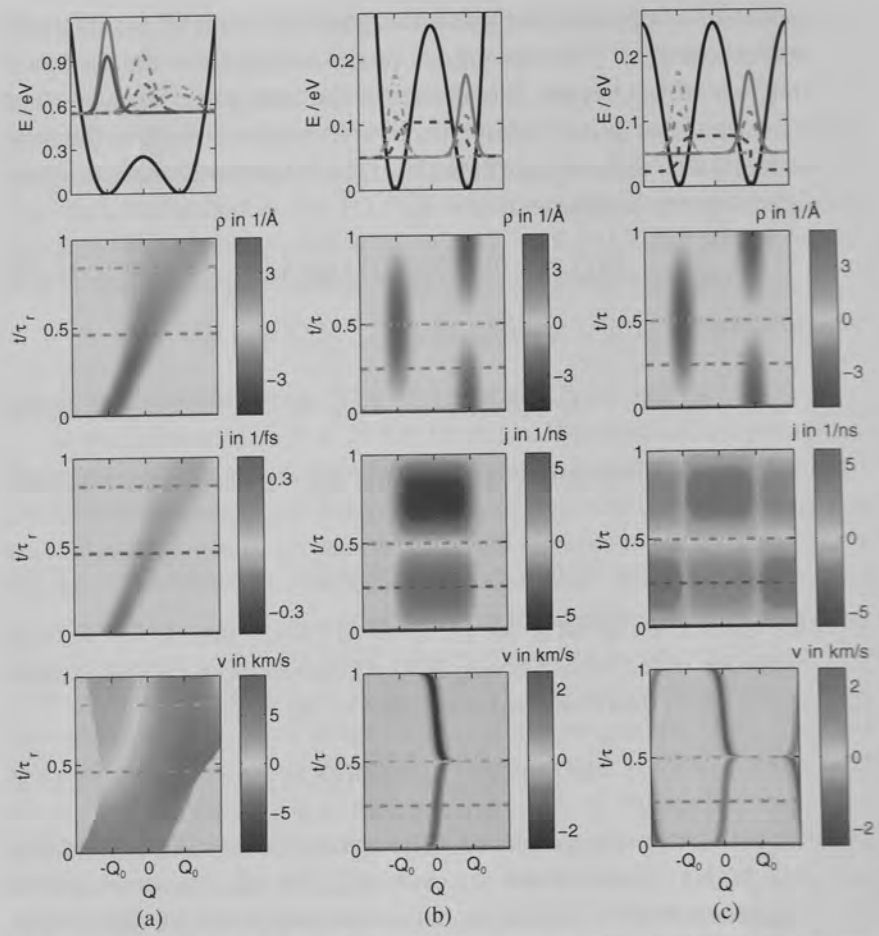

Fig. 4. Three scenarios for the 1D model of the inversion of the perdeuterated ammonia ND_3 with energy above the potential barrier (case $E > B$, (a)) or below it (tunneling domain, case $E < B$, (b)), for the familiar non-cyclic system ((a), (b)) and for an artificial version with cyclic boundary conditions (case $E < B$ only, (c)). Top panels: Three snapshots of the nuclear density $\rho(Q,t)$ and flux density $j(Q,t)$ at times $t = 0, t = \tau_r/2$ and $t = \tau_r$, where τ_r denotes the "reaction time" which is needed for reaction from reactant to product, i.e., $\tau_r = 19.3$ fs for the case $E > B$ ((a)) and $\tau_r = \tau/2$, where $\tau = 589$ ps is the tunneling time for the case $E < B$ ((b) and (c)). The densities and flux densities are embedded in the symmetric double-well potential energy curve $V(Q)$ versus the reaction coordinate Q which is approximately the difference of the positions of the nucleus of the nitrogen atom minus the center of mass of the three deuterium atoms, in C_{3v} symmetry (adapted from Ref. 92).

(Fig. 4. caption continued) The base lines of ρ and j correspond to the mean energies E. The domains of the "left" and "right" potential wells are called "reactants R" and "products P", respectively. The first, second and third rows below the top row show 2D color-coded representations of $\rho(Q,t)$, $j(Q,t)$, and of the velocity $v(Q,t) = j(Q,t)/\rho(Q,t)$ versus Q and t, respectively. The times for the snapshots shown in the top panels are indicated by horizontal lines. Note that the densities $\rho(Q,t)$ for the scenarios (b), (c) are indistinguishable on graphical scale, whereas the flux densities $j(Q,t)$ are entirely different. For figure in full color, refer to Appendix (Page 232).

contour plots of the nuclear density and flux density shown in the second- and third-from-top panels of Fig. 4(a), respectively, reveal that the time evolutions of $\rho(Q,t)$ and $j(Q,t)$ resemble each other. The ratio

$$v(Q,t) = \frac{j(Q,t)}{\rho(Q,t)} \tag{2.28}$$

defines the quantum mechanical velocity,[100–102] corresponding to the classical relation $v_{\mathrm{cl}}(t) = j_{\mathrm{cl}}(t)/\rho_{\mathrm{cl}}(t)$. This is illustrated in the bottom panel of Fig. 4(a). Apparently, the mean value of the velocity $v(Q,t)$ decreases as the wave function $\Psi(Q,t)$ climbs the potential barrier from R to B, followed by the equivalent gain of speed on the way from B to P.

Let us now investigate the nuclear flux density for energies $E < B$, that means in the so-called tunneling domain. As example, we consider the same model for the inversion of ND_3 which has already been investigated for the case $E > B$. Specifically, we assume that the initial wavepacket is the reactant superposition of the two wave functions of the tunneling doublet, Eq. (2.20). In this case, one may employ analytical expressions for the time evolutions of the wave function, density, and flux density so that it is not necessary to solve the equations of Sec. 2.2 numerically. Specifically, the solution of the TDNSE is

$$\Psi(Q,t) = \frac{1}{\sqrt{2}}(\Psi_0(Q)e^{-iE_0t/\hbar} + \Psi_1(Q)e^{-iE_1t/\hbar}), \tag{2.29}$$

implying the expressions

$$\rho(Q,t) = \frac{1}{2}(\Psi_0(Q)^2 + \Psi_1(Q)^2 + 2\Psi_0(Q)\Psi_1(Q)\cos(\omega t)) \tag{2.30}$$

and

$$j(Q,t) = \frac{\hbar}{2\mu}\left(\Psi_1(Q)\frac{\partial}{\partial Q}\Psi_0(Q) - \Psi_0(Q)\frac{\partial}{\partial Q}\Psi_1(Q)\right)\sin(\omega t) \tag{2.31}$$

for the nuclear densities and flux densities, respectively.[6,8] The tunneling frequency ω is related to the tunnel splitting ΔE and to the tunneling time τ,

$$\hbar\omega = \Delta E = E_1 - E_0 = h/\tau. \tag{2.32}$$

In the present application, $\Delta E = 7.02\times10^{-6}$ eV, thus $\tau = 589$ ps. Both quantities (2.30), (2.31) are related to each other by the reduced continuity equation for nuclear motions along Q,

$$\frac{\partial\rho(Q,t)}{\partial t} + \frac{\partial j(Q,t)}{\partial Q} = 0, \tag{2.33}$$

analogous to Eq. (2.5). Likewise, the boundary conditions

$$j(Q,t) \to 0 \quad \text{for } Q \to -\infty \quad \text{and} \quad Q \to +\infty \tag{2.34}$$

imply that

$$j(Q,t) = -\frac{\partial}{\partial t}\int_{-\infty}^{Q} dQ'\rho(Q',t), \tag{2.35}$$

cf. Eqs. (2.7) and (2.8). For numerical applications, it is more convenient to employ Eq. (2.35) than (2.31).[6,8]

The resulting reduced (1D) nuclear densities $\rho(Q,t)$ and flux densities $j(Q,t)$ are illustrated by means of snapshots and contour plots in the top as well as the first- and second-from-top panels of Fig. 4(b), respectively. Apparently, during the first half tunneling cycle, the nuclear density $\rho(Q,t)$ in the domain of R disappears while at the same time that for P emerges, without any significant population of the domain of the barrier between R and P. This familiar tunneling phenomenon is reversed during the second half tunneling period, and then it continues periodically with period ω. In sharp contrast, the nuclear flux density $j(Q,t)$ achieves its maximum value during the first half cycle of tunneling precisely below the barrier B, at $Q = 0, t = \tau/4$. During the second half period, the flux density is reversed, and then it continues periodically with period ω. The resulting tunneling velocity (2.28) is illustrated in the bottom panel of Fig. 4(b): Apparently,

its maximum value $\max(v(Q,t))$ is also achieved at $Q = 0$ and $t = \tau/4$. For comparison, in Ref. 10, we have derived an approximate analytical expression for the maximum velocity of tunneling in the so-called deep tunneling regime, that means in the limit of very high and broad potential barriers and masses (large values of V_B, Q_0 and μ which all make tunneling rather difficult),

$$\max(v(Q,t)) = \sqrt{2B/\mu}. \tag{2.36}$$

In the present case, expression (2.28) yields the numerical value $\max(v(Q,t)) = 2.99$ km/s, compared to the value 3.38 km/s for the estimate (2.36). Figure 4 shows that the value of the tunneling velocity remains rather close to its maximum value during most of the first half cycle of tunneling (during the second half cycle, the velocity is reversed), as long as the system is close to the barrier, say from $-Q_0/10$ to $+Q_0/10$. Accordingly, one can estimate the time which is needed in order to tunnel through the domain under the top of the barrier,[10]

$$t_B \approx \frac{Q_0}{5\max(v)}. \tag{2.37}$$

For the inversion tunneling of ND_3, expression (2.37) yields $t_B \approx 2.6$ fs. This is much shorter than the tunneling time $\tau = 589$ ps. This result may be interpreted as follows: There are (at least) three ways of observing tunneling. First, one may monitor the decay of the reactants or the formation of the products. The characteristic, rather long time for these processes is half the tunneling time, $\tau/2$. Alternatively, τ may be determined in terms of the tunneling splitting, $\tau = h/\Delta E$. Third, in an ideal experiment for a single molecule, one may — at least in principle — try to observe the system when it passes through the barrier, for example one may try to observe ND_3 in its planar configuration, half way between R and P. For the single molecule, this event is expected to occur once during the long time $\tau/2$, but when it happens, then the event of passing through the barrier takes only the very short time (2.37). In other words, one can say that on one hand, the system does not "like" to tunnel — that is why the tunneling time τ is rather long. On the other hand, if it tunnels, then it makes it through the barrier as fast as possible — that is why the time t_B (2.37) is so short. In physics and chemistry, there are various other time-dependent phenomena

which are characterized by long mean life times versus short durations of the individual processes, e.g., fluorescence of photoexcited molecules may take mean fluorescence lifetimes in the nanosecond or even longer time domain, whereas the event of the molecular transition from an electronic excited state to the ground state by spontaneous emission of a photon may occur in the femtosecond or even attosecond time domain.[103]

Finally, we construct a cyclic model system with identical mass μ and potential $V(Q)$ in the domain $-Q_0 < Q < +Q_0$ as for the model of inversion of ND_3, but with cyclic continuation of the double-well potential $V(\pm Q_0 + Q) = V(\pm Q_0 - Q)$, see Fig. 4(c). The corresponding energies E_0 and E_1 of the lowest tunneling doublet are almost the same as those for the non-cyclic model. As a consequence, the wave functions $\Psi_0(Q)$ and $\Psi_1(Q)$ of the cyclic and non-cyclic models are also practically the same, in the domain where the potentials $V(Q)$ are the same, $-Q_0 < Q < +Q_0$. In the complementary domains, the cyclic symmetry imposes the relations $|\Psi_i(\pm Q_0 + Q)| = |\Psi_i(\pm Q_0 - Q)|$ for the two states of the lowest tunneling doublet, $i = 0, 1$. The resulting nuclear density $\rho(Q, t)$ and flux density $j(Q, t)$ of the cyclic model are shown as snapshots in the top panel of Fig. 4(c) and as contour plots in the first- and second-from-top panels of Fig. 4(c), respectively; the velocity $v(Q, t)$ is presented in the bottom panel of Fig. 4(c). Comparison with the results presented in Fig. 4(b) shows that the nuclear densities of the cyclic and non-cyclic models are practically indistinguishable. In contrast, the flux densities of the non-cyclic (Fig. 4(b)) and cyclic (Fig. 4(c)) models are entirely different. The reason for this discrepancy are the different boundary conditions, Eq. (2.34), for the non-cyclic model versus

$$j(Q, t) = 0 \quad \text{for } Q = +Q_0 \quad \text{and} \quad \text{for } Q = -Q_0 \tag{2.38}$$

imposed by the symmetry of the cyclic model. As a consequence, Eq. (2.35) for the flux density of the non-cyclic model is modified into

$$j(Q, t) = -\frac{\partial}{\partial t} \int_{Q_0}^{Q} dQ' \rho(Q', t) \tag{2.39}$$

for the cyclic model.

The cyclic model (Fig. 4(c)) is presented here because the comparison with the non-cyclic model (Fig. 4(b)) implies three lessons: First, the information contained in the flux densities j goes in general beyond the information contained in the densities ρ. For the present reduced 1D models, one needs the densities ρ together with the proper boundary conditions in order to construct the flux densities j. In 3D, it does not even suffice to apply the continuity equation together with the proper boundary conditions, because one needs altogether three equations in order to construct the three components of j; the continuity equation is just one of them. Second, the example also sheds some general light on the robustness of the results derived from density functional theory with respect to small changes of the density: In the present case, marginal changes of the density from the non-cyclic to the cyclic models (which are below the graphical resolutions of Figs. 4(b) and 4(c)) may cause entirely different flux densities. Third, the present somewhat artificial cyclic model serves as example for more realistic models of nuclear densities and flux densities in systems with cyclic molecular motions such as torsions of two symmetric molecular fragments about a common axis, e.g., in oriented $B_2Cl_2F_2$,[8] or the cis–trans isomerization of methaniminium.[10,104]

2.4. *Nuclear flux density and induced magnetic field in pseudorotating OsH_4*[4,17] *and ReH_4^-*

In this section, we extend the previous results for reduced 1D nuclear flux densities in vibrating diatomic molecules or molecular ions (Secs. 2.1 and 2.2) or in 1D model systems with symmetric double-well potentials (Sec. 2.3) to reduced 3D flux densities of the pseudorotating central Re nucleus of the tetrahedral ReH_4^- anion. The results are analogous to those for the tetrahedral OsH_4 molecule;[4,17] the subsequent presentation summarizes the detailed derivation given in Ref. 4, with some extensions and new application to ReH_4^-.

As motivation for our choice of the systems, OsH_4[4,17] and ReH_4^-, and for the properties of their pseudorotating central nuclei, it is illuminating to consider first a classical picture. Accordingly, the term "pseudorotation" (pr) means that the central nucleus (Nu) circulates on a periodic orbit about

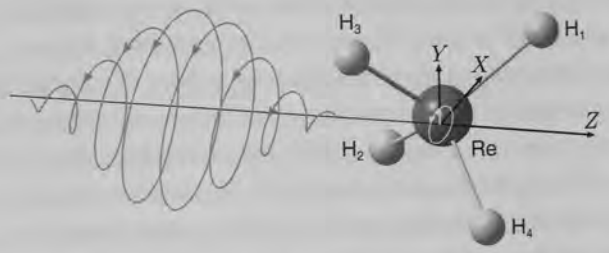

Fig. 5. Excitation of the pseudorotation of the tetrahedral anion ReH_4^- by a right-handed circularly polarized laser pulse propagating along the Z-axis (schematic). The red arrows indicate the central sequence of the laser cycles as they would be "seen" by the anion as the pulse passes by. The white straight and curvilinear arrows correspond to the vibrational stretch and pseudorotation of the central nucleus Re of ReH_4^-, respectively. The associated displacements of the four protons labeled $i = 1, \ldots, 4$ are not shown. For figure in full color, refer to Appendix (Page 233).

the molecular center of mass, with very small radius R_{pr}; this is illustrated schematically by the classical trajectory along the ring loop shown in Fig. 5. The pseudorotation gives rise to the classical ring current,

$$I = \frac{Z_{Nu}e}{T_{pr}}, \tag{2.40}$$

where $Z_{Nu}e$ denotes the nuclear charge, and T_{pr} is the period of the pseudorotation. Moreover, application of the Biot–Savart law to the ring loop model implies the induction of a magnetic field with absolute peak value at the center of the nuclear circle,[4]

$$|\mathbf{B}(\mathbf{0})| = \frac{\mu_0}{2}\frac{I}{R_{pr}} = \frac{\mu_0}{2}\frac{Z_{Nu}e}{T_{pr}R_{pr}}. \tag{2.41}$$

The choices of OsH_4[4,17] and ReH_4^- are motivated by the search for systems with strong nuclear ring currents (2.40) and induced magnetic fields (2.41). Accordingly, the corresponding ideal systems should satisfy several criteria: (i) The nuclear charge $Z_{Nu}e$ should be large, cf. Eq. (2.40). As a consequence, the mass of the central nucleus M_{nu} should be heavy. (ii) The pseudorotational period T_{pr} should be small, cf. Eq. (2.40). The associated pseudorotational frequency $\omega_{pr} = 2\pi/T_{pr}$ should, therefore, be high. (iii) The radius R_{pr} of pseudorotation should be small, cf. Eq. (2.41). (iv) Experience[11,12,14,105] shows that condition (iii) is satisfied

most efficiently if the pseudorotating central heavy nucleus (mass M_{nu}) is surrounded by light (l) peripheral ones (mass M_l), that is, the mass ratio M_{nu}/M_l should be large. Moreover, previous investigations[11,12,14,105] suggest excitation of the pseudorotation by means of a circularly polarized laser pulse, with frequency ω near resonant to ω_{pr}. Ultimately, this scenario and the criteria (i)–(iv) imply that tetrahedral metallotetrahydrides (T_d symmetry) such as OsH_4 or ReH_4^- should be rather ideal systems, see Fig. 5; for the step-by-step derivation, see Ref. 4.

The circulation of the central nucleus is associated with small amplitude motions of the surrounding protons about their tetrahedral equilibrium positions, in the rotational ground state. For convenience, we consider the scenario where the molecular center of mass is at the origin of a right-handed set of Cartesian coordinates (X, Y, Z) in the laboratory, and the periodic orbit of the central nucleus is in the XY-plane. A convenient choice of (X, Y, Z) will be specified below.

For a more rigorous classical definition of the pseudorotation, the nuclei are labeled $i = 0$ for the central nucleus Re and $i = 1-4$ for the surrounding protons, see Fig. 5. The corresponding masses are $M_0 = 186.9557\,\mathrm{u}$ for Re and $M_i = 1.0078\,\mathrm{u}$ for the hydrogen (protons) $i = 1, \ldots, 4$. The nuclear motions are described in terms of Cartesian displacements (x_i, y_i, z_i) from their classical equilibrium positions $(X_{i\mathrm{eq}}, Y_{i\mathrm{eq}}, Z_{i\mathrm{eq}})$, or by the corresponding mass-weighted coordinates $(q_{iX}, q_{iY}, q_{iZ}) = \sqrt{M_i}(x_i, y_i, z_i)$, all parallel to (X, Y, Z). In particular, for the displacements of the central nucleus from the origin $(0, 0, 0)$ of the coordinates system (X, Y, Z) we have $(x_0, y_0, z_0) = (X, Y, Z)$, thus $(q_{0X}, q_{0Y}, q_{0Z}) = \sqrt{M_0}$ (X, Y, Z). Using the $5 \times 3 = 15$ mass-weighted coordinates, one can define 15 symmetry-(T_d)-adapted coordinates Q_j, $j = 1, \ldots, 15$.[4] Three of them, called Q_{tX}, Q_{tY}, Q_{tZ} (with irreducible representation IREP t_2), describe translations (t) along X, Y, Z, respectively. Another set of three symmetry-adapted coordinates, called Q_{rX}, Q_{rY}, Q_{rZ} (with IREP t_1) describes rotations about the X-, Y- and Z- axes, respectively. The remaining $15 - 6 = 9$ symmetry-adapted coordinates describe vibrations, specifically Q_s for the symmetric stretch (with IREP a_1), Q_{b1}, Q_{b2} for the doubly degenerate bend (with 2D IREP e_1), and finally two sets of coordinates called Q_{pX}, Q_{pY}, Q_{pZ} and Q_{oX}, Q_{oY}, Q_{oZ} (with the 3D IREP t_2). Exemplarily, Q_{pX} and Q_{oX} are illustrated in Fig. 6. Apparently, they describe nuclear

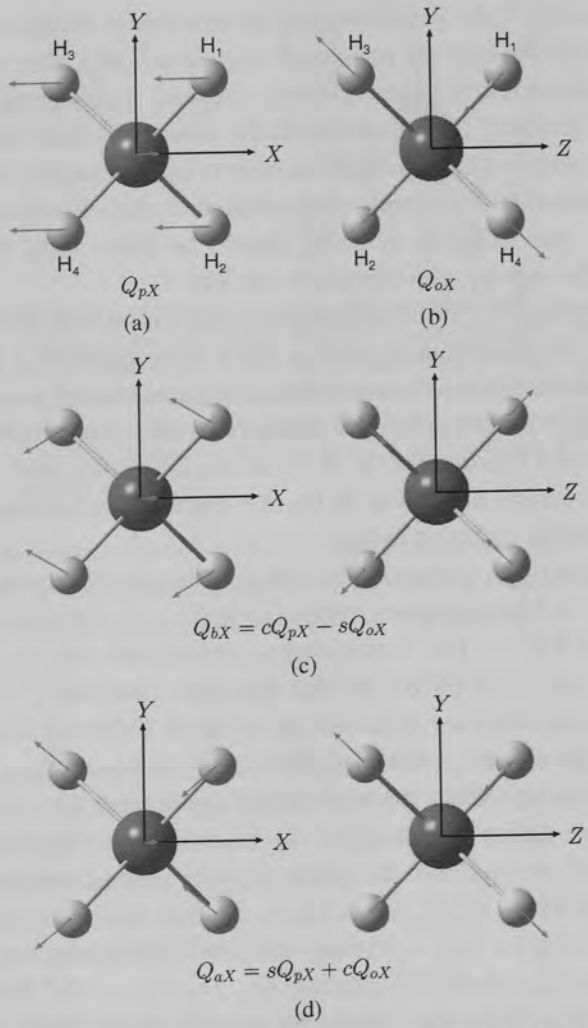

Fig. 6. Two orthonormal symmetry-adapted coordinates Q_{pX} (a) and Q_{oX} (b) belonging to the irreducible t_2 representation (IREP) of the point group T_d of the ReH_4^- anion; they describe nuclear motions parallel ("p") and orthogonal ("o") to the X-axis, respectively. Their superpositions (c) and (d) with coefficients $c = \cos(\eta)$ and $s = \sin(\eta)$ and mixing angle $\eta = 39.8°$ correspond to the X-components of the triply degenerate bend ("b") and antisymmetric stretch ("a"), with the same IREP t_2. The arrows indicate the nuclear displacements (not to scale); the displacements of the heavy central nucleus are enlarged by a factor 20. The left and right columns show different views of the coordinates along the Z- and negative X-directions, respectively. The corresponding sets of Y- and Z-components of symmetry-adapted and normal mode coordinates are analogous, but not shown. For figure in full color, refer to Appendix (Page 234).

motions parallel (p) and orthogonal (o) to X, hence they are called Q_{pX} and Q_{oX}, respectively. By T_d symmetry, Q_{pY}, Q_{oY} and Q_{pZ}, Q_{oZ} are analogous coordinates describing nuclear motions parallel and orthogonal to Y and Z, respectively. Figure 6 also shows two orthogonal linear combinations of Q_{pX} and Q_{oX},

$$\begin{aligned} Q_{bX} &= \cos(\eta)Q_{pX} - \sin(\eta)Q_{oX}, \\ Q_{aX} &= \sin(\eta)Q_{pX} + \cos(\eta)Q_{oX}, \end{aligned} \tag{2.42}$$

with so-called *mixing angle* η, where $\eta = 39.8°$ for ReH_4^-. These are the X-components of the triply degenerate bend ("b") and antisymmetric stretch ("a") t_2 normal modes, respectively. Obviously, they describe vibrations of the central Re nucleus along the X-direction, together with complementary motions of the surrounding protons. The corresponding Y- and Z-components are constructed as analogous linear combinations of the Q_{pY}, Q_{oY} and Q_{pZ}, Q_{oZ} modes, respectively. Classical pseudorotations in the triply degenerate bend or antisymmetric stretch modes about the Z-axis, in the XY-plane, are constructed as superpositions of the perpendicular X- and Y-components of either the triply degenerate bend, or the antisymmetric stretch, with phase shift $\pi/2$. In Refs. 4, 17 for OsH_4, we have centered attention on the bend (Fig. 6(c)). As an alternative, the present investigation of ReH_4^- focuses on the antisymmetric stretch (Fig. 6(d)). Accordingly, the classical time evolutions of the Cartesian coordinates are

$$\begin{aligned} Q_{aX}(t) &= Q_a \cos(\omega_a t), \\ Q_{aY}(t) &= Q_a \sin(\omega_a t), \\ Q_{aZ}(t) &= 0, \end{aligned} \tag{2.43}$$

for right-handed pseudorotation about the Z-axis, with amplitude Q_a and normal mode frequency ω_a. It is convenient to describe these pseudorotations in terms of corresponding cylindrical coordinates with radial, angular and Z- components Q_a and δ_a, Q_{aZ}, such that

$$\begin{aligned} Q_{aX} &= Q_a \cos(\delta_a), \\ Q_{aY} &= Q_a \sin(\delta_a), \\ Q_{aZ} &= 0. \end{aligned} \tag{2.44}$$

The corresponding classical time evolutions of the cylindrical coordinates are given by

$$\begin{aligned} Q_a(t) &= \sqrt{(Q_{aX}(t)^2 + Q_{aY}(t)^2)} = Q_a = \text{const}, \\ \delta_a(t) &= \omega_a t, \\ Q_{aZ}(t) &= 0. \end{aligned} \tag{2.45}$$

Analogous pseudorotations about any other axis can be constructed by means of corresponding superpositions of the normal mode vibrations along coordinates Q_{aX}, Q_{aY} and Q_{aZ}.

The frequencies ω_a for the pseudorotations and for the other vibrations are calculated by means of quantum chemical *ab initio* methods. Specifically, the optimized structures of ReH_4^- and harmonic frequencies are obtained by means of the analytical gradient and Hessian techniques at the complete active space self-consistent field (CASSCF)[106] level and by a numerical approach at the level of complete active space perturbation theory 2nd order (CASPT2),[107,108] under C_{2v} symmetry as subgroup of D_{2d} and T_d point group symmetry with the following relativistic atomic natural orbitals basis sets: [24s, 21p, 15d, 11f, 4g, 2h] primitive contracted into (6s, 5p, 3d, 1f) for the Rhenium atom and [6s, 4p, 3d, 1f] contracted to (3s, 2p, 1d) for the hydrogen atom.[109] Scalar relativistic effects were described using a Douglas–Kroll–Hess Hamiltonian.[110,111] The CASSCF calculations were performed for the electronic ground state of ReH_4^- in C_{2v} point group symmetry. Twelve electrons were correlated in 12 active orbitals including the 5d orbitals of the Rhenium. The *ab initio* calculations were performed with the `Molcas 7.0` quantum chemistry software.[112] Whatever the initial symmetry is (belonging to the T_d or D_{2d} point group symmetry), the structure optimization converges to a structure belonging to T_d symmetry at the CASSCF and CASPT2 levels. At the CASPT2 level the Re–H bond length is 1.622 Å, and the bond angle is 109.47°. The following normal modes characterized ReH_4^- in its electronic ground state: (i) two t_2 modes calculated at 820 cm^{-1} and 2008 cm^{-1} corresponding to the bending and antisymmetric stretching modes, respectively; (ii) one e mode calculated at 250 cm^{-1}; (iii) one a_1 mode calculated at 2109 cm^{-1}.

A convenient definition of the laboratory-fixed Cartesian (X, Y, Z) coordinates, together with the definition of the "time zero", $t = 0$, is

motivated by excitation of the pseudorotations of the central nucleus by means of a right (+) or left (−) circularly polarized laser pulse, with frequency ω near-resonant to ω_a; exemplarily, we consider the case "+", see Fig. 5. Accordingly, the direction of propagation of the laser pulse defines the coordinate Z. The "time zero" is defined as the time when the laser pulse achieves its maximum intensity. The coordinate X is defined by the direction of the electric field of the laser pulse at $t = 0$. Finally, Y is perpendicular to X and Z such that (X, Y, Z) forms a right-handed set of Cartesian coordinates.

Explicitly, the electric field components are defined in terms of the vector potential

$$\begin{pmatrix} \mathcal{E}_X(t) \\ \mathcal{E}_Y(t) \\ 0 \end{pmatrix} = -\frac{d}{dt} \begin{pmatrix} A_X(t) \\ A_Y(t) \\ 0 \end{pmatrix}, \tag{2.46}$$

where

$$\begin{pmatrix} A_X(t) \\ A_Y(t) \\ 0 \end{pmatrix} = -\frac{\mathcal{E}_0}{\omega} s(t) \begin{pmatrix} \sin(\omega t) \\ -\cos(\omega t) \\ 0 \end{pmatrix}, \tag{2.47}$$

with laser frequency ω near resonant to the pseudorotational frequency ω_a, field strength $\mathcal{E}_0$ and shape function

$$s(t) = \begin{cases} \cos^n\left(\dfrac{\pi t}{t_p}\right) & \text{for } |t| \leq \dfrac{t_p}{2}, \\ 0 & \text{for } |t| > \dfrac{t_p}{2}, \end{cases} \tag{2.48}$$

implying $\mathcal{E}_Y(t = 0) = 0$. In the present application, we set $n = 20$ such that $s(t)$ approaches a Gaussian function very well.[113] The time-dependent intensity

$$I(t) = c\epsilon_0 |\mathcal{E}(t)|^2 \tag{2.49}$$

is then approximately given by

$$I(t) \approx c\varepsilon_0 \mathcal{E}_0^2 s^2(t). \tag{2.50}$$

In the semiclassical dipole approximation, the electric field components $\mathcal{E}_X(t)$ and $\mathcal{E}_Y(t)$ are coupled to the X- and Y-dipole components M_X and M_Y of the systems, respectively, with contribution $-M_X\mathcal{E}_X(t) - M_Y\mathcal{E}_Y(t)$ to the system's Hamiltonian. For the present application, we make use of the T_d-symmetry-adapted representations of the dipole components. Using the linear approximation, also called "electric harmonicity", the relevant terms which enable the excitations of the pseudorotations are

$$M_X(Q_{bX}, Q_{aX}) = \left.\frac{\partial M_X}{\partial Q_{bX}}\right|_{Q_{bX}=0} Q_{bX} + \left.\frac{\partial M_X}{\partial Q_{aX}}\right|_{Q_{aX}=0} Q_{aX} \tag{2.51}$$

and

$$M_Y(Q_{bY}, Q_{aY}) = \left.\frac{\partial M_Y}{\partial Q_{bY}}\right|_{Q_{bY}=0} Q_{bY} + \left.\frac{\partial M_Y}{\partial Q_{aY}}\right|_{Q_{aY}=0} Q_{aY}. \tag{2.52}$$

The partial derivatives $\frac{\partial M_X}{\partial Q_{bX}}|_{Q_{bX}=0}$, etc., are evaluated by means of the same *ab initio* methods of quantum chemistry which have been specified above.

Figures 7(a,b) show the corresponding X- and Y-components of the electric field of the laser pulse, together with its intensity. The laser parameters are specified in the legend of Fig. 7; they are optimized such that the laser pulse achieves mode-selective excitation of the target pseudorotation. As explained above, in the classical picture this corresponds to the superposition of the X- and Y-components of the triply degenerate antisymmetric stretch, with phase shift $\pi/2$. Quantum mechanically, the pseudorotations are quantized, calling for state selective optimizations of the laser parameters. In the application below, the laser pulse induces the selective transition from the vibrational ground state to the first right-handed pseudorotational excited state which is associated with the triply degenerate antisymmetric stretch. The quantum mechanical representation of these and other states is explained below, together with the associated nuclear flux densities. We shall also discuss the magnetic fields which are induced by these flux densities.

For low excitations, the nuclear eigenstates of the tetrahedral OsH_4[4,17] or ReH_4^- can be described in terms of products of translational (t), rotational (r) and vibrational (v) wave functions depending on the cylindrical versions

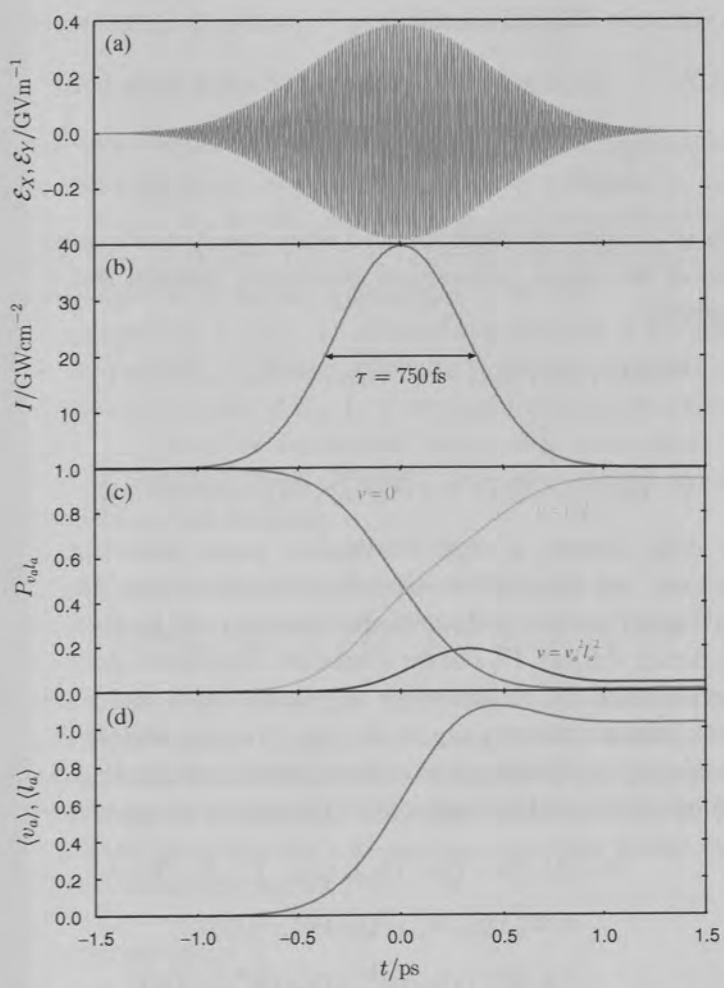

Fig. 7. Selective excitation of the ReH_4^- anion from the vibrational ground state $v = 0$ to the first excited right-handed pseudorotational state $v_a^1 l_a^1$, by means of a right circularly polarized laser pulse with $\cos^{20}$ envelope, cf. Fig. 5. (a) The X-(red) and Y-(green) components of the electric field with amplitude $\mathcal{E}_0 = 0.387$ GV/m, laser frequency $\omega = 2005\ 2\pi c\,\mathrm{cm}^{-1}$ and effective pulse duration $\tau = 750$ fs. (b) The corresponding time-dependent intensity $I(t)$ with its maximum $I_{\max} = 39.8\,\mathrm{GV/cm}^2$. (c) The resulting populations of the dominant vibrational states $v = 0, v = v_a^1 l_a^1$ and $v = v_a^2 l_a^2$. Other vibrational states have negligible populations. (d) The mean quantum numbers for the antisymmetric stretch $\langle v_a(t) \rangle$ and for the corresponding pseudorotation $\langle l_a(t) \rangle$ — they coincide on graphical scale. For figure in full color, refer to Appendix (Page 235).

of the symmetry-adapted coordinates,

$$\Psi_{t,r,v}(Q_1,\ldots,Q_{15}) = \Psi_t(Q_{tX},Q_{tY},Q_{tZ})\Psi_r(Q_{rX},Q_{rY},Q_{rZ}) \times \Psi_v(Q_s,Q_{b1},Q_{b2},Q_{bZ},Q_{aZ},Q_b,\delta_b,Q_a,\delta_a). \tag{2.53}$$

Let us consider the ideal scenario where the system's center of mass is fixed at the origin, without any translation, rotation and dispersion. Accordingly

$$\Psi_t(Q_{tX},Q_{tY},Q_{tZ}) = \sqrt{\delta(Q_{tX})}\sqrt{\delta(Q_{tY})}\sqrt{\delta(Q_{tZ})} \tag{2.54}$$

and

$$\Psi_r(Q_{tX},Q_{tY},Q_{tZ}) = \sqrt{\delta(Q_{rX})}\sqrt{\delta(Q_{rY})}\sqrt{\delta(Q_{rZ})}, \tag{2.55}$$

where $\delta(Q)$ denotes a delta-distribution. Some important effects of translational and rotational wavepacket dispersions (beyond the present approximation in terms of the delta distributions) will be discussed below, for the details see Ref. 17. For the vibrations (symmetric stretch s, doubly degenerate bends $b1, b2$, and triply degenerate bends and antisymmetric stretches, with notations $b_Z, a_Z, b, \delta_b, a, \delta_a$, corresponding to the cylindrical versions of the T_d-symmetry-adapted vibrational coordinates) we have in harmonic (indicated by superscript h) normal mode approximation

$$\begin{aligned}\Psi_v(Q_s,Q_{b1},Q_{b2},Q_{bZ},Q_{aZ},Q_b,\delta_b,Q_a,\delta_a) &= \Phi^h_{v_s}(Q_s)\Phi^h_{v_{b1}}(Q_{b1})\Phi^h_{v_{b2}}(Q_{b2}) \\ &\times \Phi^h_{v_{bZ}}(Q_{bZ})\Phi^h_{v_{aZ}}(Q_{aZ})\Phi^h_{v_b|l_b|}(Q_b) \\ &\times \Phi^h_{l_b}(\delta_b)\Phi^h_{v_a|l_a|}(Q_b)\Phi^h_{l_a}(\delta_a),\end{aligned} \tag{2.56}$$

where $\Phi^h_v(Q)$ and $\Phi^h_{v|l|}(Q)\Phi_l(\delta)$ denote 1D and 2D harmonic oscillator wave functions, respectively[4] (adapted from Ref. 114). In particular,

$$\Phi^h_{l_a}(\delta_a) = \frac{1}{\sqrt{2\pi}}e^{il_a\delta_a} \tag{2.57}$$

accounts for the antisymmetric pseudorotational motion about the Z-axis, along the angle δ_a, with quantum number l_a. The set of all vibrational

quantum numbers is, in general,

$$v = (v_s, v_{b1}, v_{b2}, v_{bZ}, v_{aZ}, v_b, l_b, v_a, l_a). \tag{2.58}$$

For special cases which are important for the present applications, we shall also use convenient shorthand notations, in particular $v = 0 = (0, 0, 0, 0, 0, 0, 0, 0, 0)$ for the vibrational and pseudorotational ground state, $v = v_a^1 l_a^1 = (0, 0, 0, 0, 0, 0, 0, 1, 1)$ for the first excited right-handed pseudorotational state of the antisymmetric t_2 mode, etc.

The corresponding $5 \times 3 = 15$-dimensional densities of the states for the five nuclei $i = 0, 1, \ldots, 4$ are also labeled by quantum numbers v. They may be evaluated in terms of the 15 Cartesian displacement coordinates $\rho_v(x_0, y_0, \ldots, z_4)$ with six constraints (trans, rot), hence they can be transformed to only nine mass-weighted symmetry-adapted coordinates (without translation and rotation),

$$\begin{aligned}\rho_v(Q_s, Q_{b1}, Q_{b2}, Q_{bZ}, Q_{aZ}, Q_b, \delta_b, Q_a, \delta_a)\\ = |\Psi_v(Q_s, Q_{b1}, Q_{b2}, Q_{bZ}, Q_{aZ}, Q_b, \delta_b, Q_a, \delta_a)|^2.\end{aligned} \tag{2.59}$$

These shall now be reduced to the densities $\tilde{\rho}_{0v}(q_{0X}, q_{0Y}, q_{0Z})$ of the central nucleus ($i = 0$), also depending on the quantum number v. By analogy with the reduction (2.1), the reduced $\tilde{\rho}_{0v}(q_{0X}, q_{0Y}, q_{0Z})$ are obtained by integrating $\rho_v(Q_s, Q_{b1}, Q_{b2}, Q_{bZ}, Q_{aZ}, Q_b, \delta_b, Q_a, \delta_a)$ over all variables complementary to q_{0X}, q_{0Y}, q_{0Z}, that means over the coordinates of all the other nuclei, $i = 1 - 4$

$$\begin{aligned}\tilde{\rho}_{0v}(q_{0X}, q_{0Y}, q_{0Z})\\ = \int dq_{1X} \int dq_{1Y} \cdots \int dq_{4Z} \rho_v(Q_s, Q_{b1}, Q_{b2}, Q_{bZ},\\ Q_{aZ}, Q_b, \delta_b, Q_a, \delta_a).\end{aligned} \tag{2.60}$$

This 12-dimensional integral has been carried out analytically.[4] Finally, the results are converted from mass-weighted coordinates q_{0X}, q_{0Y}, q_{0Z} back to the displacement coordinates $(x_0, y_0, z_0) = (X, Y, Z)$ of the central nucleus,

$$\tilde{\rho}_{0v}(X, Y, Z) = M_0^{3/2} \tilde{\rho}_{0v}(q_{0X}, q_{0Y}, q_{0Z}). \tag{2.61}$$

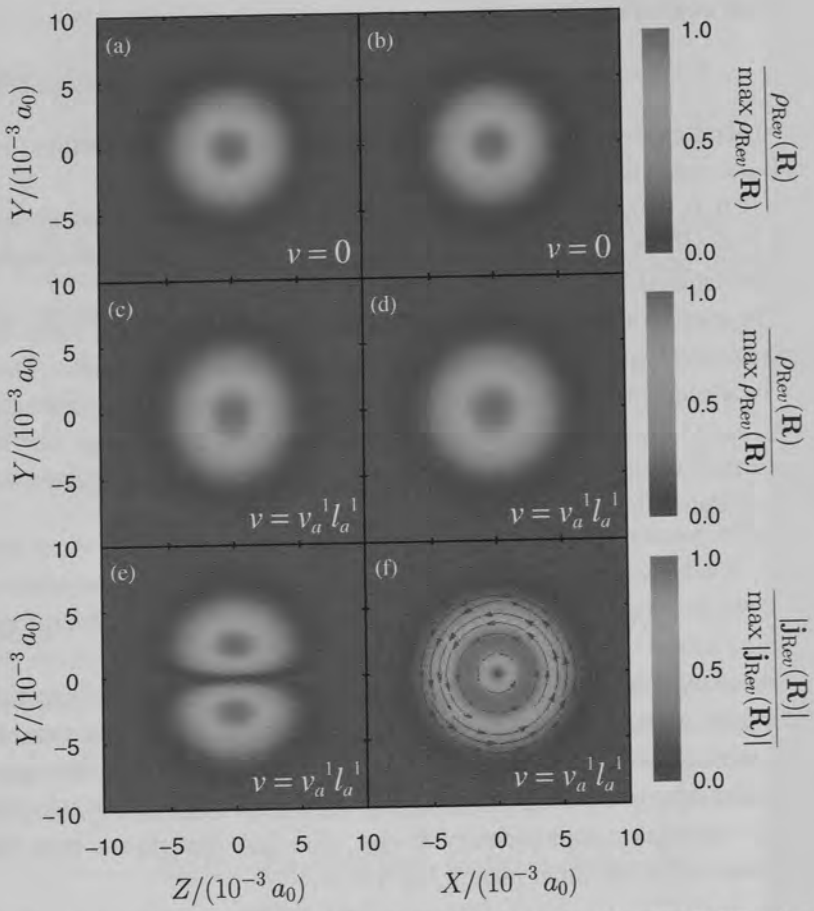

Fig. 8. Nuclear probability densities $\tilde{\rho}_{0v}(X, Y, Z)$ of the nucleus Re of the ReH_4^- anion for the vibrational ground state $v = 0$ (a), (b) (spherically symmetric) and for the first excited right-handed antisymmetric pseudorotational state $v = v_a^1 l_a^1$ (c), (d) (ellipsoidal, axially symmetric), as well as the nuclear current density $\tilde{\mathbf{j}}_{0v}(X, Y, Z)$ (axially symmetric) in the YZ-plane (a), (c), (e) and in the XY-plane (b), (d), (f). The direction of the ring current is indicated by arrows in panel (f). The corresponding electric ring current of the nucleus Re for the pseudorotational state $v_a^1 l_a^1$ is 161 $\mu A \approx 1\, e/\mathrm{fs}$, and the corresponding mean current radius is $0.0031 a_0$. For figure in full color, refer to Appendix (Page 236).

Figure 8 illustrates the resulting spherical and ellipsoidal densities $\tilde{\rho}_{00}(X, Y, Z)$ and $\tilde{\rho}_{0v_a^1 l_a^1}(X, Y, Z)$ of ReH_4^- in its vibrational ground state $v = 0$ and in the first excited antisymmetric pseudorotational target state $v = v_a^1 l_a^1$, before and after excitation by the circularly polarized laser pulse,

respectively. Figure 7 shows the corresponding state-selective excitation of this target state by means of the circularly polarized laser pulse, in terms of the populations of the target state $v_a^1 l_a^1$ and other (competing) states, as well as the mean values $\langle v_a \rangle$ and $\langle l_a \rangle$ of the quantum numbers v_a and l_a which are associated with the pseudorotation of the central nucleus in the triply degenerate antisymmetric stretch. Apparently, the target state is populated with almost 100% at the end of the laser pulse. The method for the design of the laser pulse as so-called *re-optimized π-pulse*, with corresponding optimal parameters, is adapted from Ref. 14 (see also Ref. 23). The net result may be interpreted by saying that the (right-handed) helicity of the photons propagating along Z is transferred into right-handed pseudorotations of the central nucleus about the Z-axis. The nuclear flux density of all the nuclei $i = 0, 1, \ldots, 4$ with masses M_i has $5 \times 3 = 15$ components in terms of the Cartesian displacement coordinates that is

$$\begin{aligned}
\mathbf{j}_v(x_0, y_0, \ldots, z_4) &= \begin{pmatrix} j_{v1}(x_0, y_0, \ldots, z_4) \\ j_{v2}(x_0, y_0, \ldots, z_4) \\ \vdots \\ j_{v15}(x_0, y_0, \ldots, z_4) \end{pmatrix} \\
&= \begin{pmatrix} -i\hbar/(2M_0)(\Psi_{trv}^{h*}(\partial/\partial x_0)\Psi_{trv}^{h} - \Psi_{trv}^{h}(\partial/\partial x_0)\Psi_{trv}^{h*}) \\ -i\hbar/(2M_0)(\Psi_{trv}^{h*}(\partial/\partial y_0)\Psi_{trv}^{h} - \Psi_{trv}^{h}(\partial/\partial y_0)\Psi_{trv}^{h*}) \\ \vdots \\ -i\hbar/(2M_4)(\Psi_{trv}^{h*}(\partial/\partial z_4)\Psi_{trv}^{h} - \Psi_{trv}^{h}(\partial/\partial z_4)\Psi_{trv}^{h*}) \end{pmatrix}.
\end{aligned} \tag{2.62}$$

The related continuity equation reads

$$\frac{\partial}{\partial t}\rho_v(x_0, y_0, \ldots, z_4) + \nabla_{15}\mathbf{j}_v(x_0, y_0, \ldots, z_4) = 0, \tag{2.63}$$

where ∇_{15} has 15 components,

$$\nabla_{15} = (\partial/\partial x_0, \partial/\partial y_0, \ldots, \partial/\partial z_4). \tag{2.64}$$

Subsequently, we shall focus on the corresponding reduced version of the continuity equation for the central nucleus, depending on the coordinates

$(x_0, y_0, z_0) = (X, Y, Z)$. It is obtained by integrating the 15-dimensional continuity equation over all the other coordinates $x_1, y_1, \ldots, z_4$,

$$\frac{\partial}{\partial t}\int_{-\infty}^{+\infty} dx_1 \cdots \int_{-\infty}^{+\infty} dz_4 \rho(x_0, y_0, \ldots, z_4) + \int_{-\infty}^{+\infty} dx_1 \cdots \int_{-\infty}^{+\infty} dz_4 \nabla_{15}\mathbf{j}_v(x_0, y_0, \ldots, z_4) = 0. \quad (2.65)$$

The first term yields the time derivative of the reduced density of the central nucleus, $\partial\tilde{\rho_{0v}}(X, Y, Z)/\partial t$. The second term can be written as sum of 15 integrals $\int_{-\infty}^{+\infty} dx_1 \cdots \int_{-\infty}^{+\infty} dz_4$ of the terms $\partial j_{v1}(x_0, y_0, \ldots, z_4)/\partial x_0, \ldots, \partial j_{v15}(x_0, y_0, \ldots, z_4)/\partial z_4$. Gratifyingly, all contributions for the nuclei $i = 1, \ldots, 4$ vanish upon integration, because the corresponding flux densities vanish at the boundaries of the integration; for example

$$\int_{-\infty}^{+\infty} dx_1 \partial j_{v4}(x_0, y_0, \ldots, z_4)/\partial x_1 = j_{v4}(x_0, y_0, z_0, x_1 \to +\infty, y_1, \ldots, z_4) - j_{v4}(x_0, y_0, z_0, x_1 \to -\infty, y_1, \ldots, z_4) = 0. \quad (2.66)$$

Hence, the second term of the reduced continuity equation is reduced to the contributions for the central nucleus,

$$\partial/\partial t\tilde{\rho}_{0v}(X, Y, Z) + (\partial/\partial X, \partial/\partial Y, \partial/\partial Z)\tilde{\mathbf{j}}_{0v}(X, Y, Z) = 0, \quad (2.67)$$

where the X, Y, Z-components of the reduced flux density are obtained by integrating the first three components $j_{v1}(x_0, y_0, \ldots, z_4), \ldots, j_{v3}(x_0, y_0, \ldots, z_4)$ of the 15-dimensional flux density for all nuclei over the variables of nuclei $1, \ldots, 4$. These integrals will be considered in more detail below.

In practice, $\mathbf{j}_v(x_0, y_0, \ldots, z_4)$ is first converted into mass-weighted coordinates[4]

$$\mathbf{j}_v(q_{0X}, q_{0Y}, \ldots, q_{4Z}) = \mathbf{j}_v(x_0, y_0, \ldots, z_4)/(M_0^2 M_1^8). \quad (2.68)$$

This facilitates the subsequent analytical derivations.

In the nuclear ground state $v = 0$ where $l_a = l_b = 0$, the wave functions $\Psi_{trv=0}$ is real, hence the flux density is equal to zero,

$$\mathbf{j}_{v=0}(q_{0X}, q_{0Y}, \ldots, q_{4Z}) = \mathbf{0}. \tag{2.69}$$

In contrast, the wave function $\Psi_{trv=v_a^1 l_a^1}$ representing the first excited pseudorotational state $v = v_a^1 l_a^1$ is complex. As a consequence, the 15-dimensional $\mathbf{j}_{v=v_a^1 l_a^1}(q_{0X}, q_{0Y}, \ldots, q_{4Z})$ has non-vanishing components for all the nuclei. Each of these components also depends on the coordinates of all the nuclei. The quantum mechanical evaluation, and also the corresponding (hypothetical) experimental measurement of the 15-dimensional nuclear flux density is beyond our present interest, and also beyond the available capabilities. Instead, we focus on the much simpler reduced flux density $\mathbf{j}_{0v}(q_{0X}, q_{0Y}, q_{0Z})$ of the central nucleus $i = 0$, in the given quantum state v. This is obtained by integrating $\mathbf{j}_{v=v_a^1 l_a^1}(q_{0X}, q_{0Y}, \ldots, q_{4Z})$ over all mass-weighted coordinates of the nuclei $i = 1, \ldots, 4$. Again, these integrals can be carried out analytically.[4] Finally, the results are back-converted from mass-weighted coordinates q_{0X}, q_{0Y}, q_{0Z} to Cartesian displacements from the center of mass,

$$\mathbf{j}_{0v}(X, Y, Z) = M_0^2 \mathbf{j}_{0v}(q_{0X}, q_{0Y}, q_{0Z}). \tag{2.70}$$

The resulting nuclear reduced flux density of the central nucleus in the first excited pseudorotational state $v = v_a^1 l_a^1$ is shown in Fig. 8(f). Apparently, $\mathbf{j}_{0v=v_a^1 l_a^1}(X, Y, Z)$ describes a right-handed current density of the central nucleus about the Z-axis, centered near the classical ring loop with extremely small radius, $R_{v_a^1 l_a^1} = 0.0031 a_0$. Integration of the flux density over a half-plane from the Z-axis to infinity yields the rather large nuclear electric current, $I_{v_a^1 l_a^1} = 161\ \mu A \approx 1\, e/\text{fs}$.

The magnetic field which is induced by the nuclear flux density $\mathbf{j}_{0v}(X, Y, Z)$ of the pseudorotating central nucleus (labeled "0") in vibrational/pseudorotational state v is evaluated by means of the Biot–Savart law,

$$\mathbf{B}_{0v}(\mathbf{R}) = \frac{Z_0 e \mu_0}{4\pi} \int_0^\infty d\rho' \rho' \int_{-\infty}^\infty dZ' \int_0^{2\pi} d\phi' \frac{\mathbf{j}_{0v}(\mathbf{R}') \times (\mathbf{R} - \mathbf{R}')}{|\mathbf{R} - \mathbf{R}'|^3}. \tag{2.71}$$

The integral (2.71) is carried out conveniently in terms of the cylindrical versions (ρ, ϕ, Z) of the laboratory fixed coordinates,[4] related to the Cartesian version by

$$\begin{aligned} X &= \rho\cos(\phi), \\ Y &= \rho\sin(\phi), \\ Z &= Z. \end{aligned} \tag{2.72}$$

For the first excited right-handed antisymmetric pseudorotational state $v = v_a^1 l_a^1$, the resulting magnetic field $\mathbf{B}_{0,v=v_a^1 l_a^1}(X, Y, Z)$ (not shown) resembles the magnetic field which is induced by a classical current with magnitude $I = I_{v_a^1 l_a^1} \approx 1e/\text{fs}$ in a ring loop in the XY-plane about the origin of the coordinate system, with radius $R = R_{v_a^1 l_a^1} = 0.0031a_0$. It has its maximum absolute value at the origin; for ReH_4^- it is $|\mathbf{B}_{0,v=v_a^1 l_a^1}(0,0,0)| = 405\,\text{T}$. For comparison, the value for OsH_4 is $|\mathbf{B}_{0,v=v_b^1 l_b^1}(0,0,0)| = 623\,\text{T}$.[4] This confirms the previous conjecture that for $\eta < 45°$, excitations of $v = v_b^1 l_b^1$ generate larger magnetic fields than $v = v_a^1 l_a^1$.[4]

The results for the pseudorotating ReH_4^- shown in Figs. 5–8 are obtained for the ideal scenario where the translational and rotational wave functions are represented by delta-distributions, Eqs. (2.54) and (2.55), corresponding to zero translation, zero rotation, and zero dispersion. In reality, any wave function which is highly peaked initially will disperse rapidly. Effects of wavepacket dispersion on nuclear flux densities and induced magnetic fields of pseudorotational tetrahedral metallotetrahydrides have been investigated in great detail.[17] Suffice it here to say that in the gas phase, the dispersion of the wave function representing the center of mass causes corresponding dispersion of the current density of the central nucleus which is pseudorotating about the center of mass, and consequently also dispersion of the induced magnetic field. For example, the ideal maximum value of the magnetic field $|\mathbf{B}_{0,v=v_a^1 l_a^1}(0,0,0)| = 405\,\text{T}$ of ReH_4^- in its first excited pseudorotational state $v = v_{a^1 l_a^1}$ will decay rapidly, due to dispersion of the translational wave function. In contrast, if the ReH_4^- anion is embedded in an inert matrix, wavepacket dispersion of the central Re nucleus is blocked by the surrounding rare gas atoms, such that one may expect a rather large value of $|\mathbf{B}_{0,v=v_a^1 l_a^1}(0,0,0)|$, albeit smaller than 405 T. To monitor the effect, Ref. 4 proposes an IR-pump-X-ray-probe

versus an X-ray-probe-only experiment, at the K- and L-edges of X-ray ionization.

3. Conclusions

This survey summarizes some phenomena of reduced intramolecular nuclear flux densities during adiabatic processes — vibrations and model reactions — which we have discovered, together with our co-authors, during the years 2012–2014,[4–10] see also Refs. 11–19. Exemplarily, Secs. 2.1–2.4 report upon the first nuclear flux densities in vibrating diatomic molecules or ions derived from experimental pump probe spectra, revealing new quantum effects such as the "quantum accordion" (Fig. 1); the extension of wavepacket interferometry from nuclear densities to nuclear flux densities, again with the discovery of new quantum effects which cause those interferences, for example the separation of a vibrating wave function into two partial waves which run towards opposite directions (Fig. 2); explorations of reduced nuclear flux densities during tunneling in 1D double-well potentials, with the surprising effect that these flux densities have maximum values just below the potential barrier (i.e., where the densities have their minimum values, Fig. 4); and last but not least, laser excitation of reduced nuclear flux densities of the pseudorotating central nuclei of metallotetrahydrides with T_d symmetry, inducing huge intramolecular magnetic fields (Fig. 8). Figures 1–8 present new applications, or new versions of presentations related to the results which have been presented in the original publications.[4–10] The wealth of discoveries suggests that after lying dormant for many years, the field of reduced nuclear flux densities is now awakening. The coming years will witness growth in the field, with many more discoveries.

One common theme in Secs. 2.1–2.4 has been the role of the reduced continuity equations which connect the reduced nuclear densities and flux densities. Sec. 2.4 presents an example for the reduction of the "original", high-dimensional (here: 15D) continuity equation for all the nuclei (which is a consequence of the time-dependent Schrödinger equation[4]), to the 3D reduced continuity equation of a specific, single nucleus. At the same time, the original nuclear densities and flux densities which depend on the variables (here: 15) of all the nuclei are reduced to the 3D densities

and flux densities of a single nucleus. Section 2.1 shows how the 3D nuclear continuity equation for the densities and flux densities of diatomic systems, depending on three components of the internuclear vector, is reduced further to the 1D continuity equation for the reduced densities and flux densities of nothing but the bond length. It is important to note that the continuity equations, or the reduced continuity equations are partial differential equations, i.e., they link the (reduced) densities and flux densities to each other, but knowledge of one of them (e.g., the densities) is by no means sufficient for evaluating the other one (e.g., the flux density). Sections 2.1 and 2.2 show that even in the case of applications to the rather simple 1D systems, e.g., pure vibrations of diatomic molecules or ions, the differential equation, i.e., the reduced continuity equation, has to be supplemented by the proper boundary conditions, in order to enable the evaluations of the quantum nuclear flux densities in terms of the densities. Section 2.3 demonstrates a spectacular example where practically the same reduced nuclear densities (indistinguishable on the graphical scale) yield entirely different reduced nuclear flux densities, depending on the different boundary conditions for tunneling in non-cyclic versus cyclic double-well potentials, cf. Fig. 4. In the more demanding case of 3D intramolecular densities and flux densities of selected nuclei, the results of Sec. 2.4 imply that the corresponding reduced continuity equation does not suffice at all in order to relate the densities to the flux densities. In the specific example, a circularly polarized laser pulse excites an intramolecular nuclear ring current which is represented by an excited eigenstate. After the laser pulse, the reduced nuclear density of the eigenstate is stationary, hence its time derivative is equal to zero. As a consequence, the reduced continuity equation implies that the divergence of the reduced nuclear flux density is also equal to zero. Two components of the flux density vanish anyway (i.e., the radial component and the component along the symmetry axis Z), for symmetry reasons.[4] Ultimately, the reduced continuity equation implies, therefore, that the angular component of the reduced flux density is stationary. This is confirmed in Fig. 8, i.e., the reduced internuclear flux density has axial symmetry — it does not depend on the cylindrical angular variable. But the reduced continuity equation *per se* cannot predict the shape of the angular component of the reduced flux density depending on the two other variables. Instead, they have been evaluated by a rather

irksome procedure,[4] starting from the original definition of the nuclear flux density for all nuclei in full dimensionality (here: 15D), and then reducing it to the flux density of a specific nucleus (here: the central one) by integrating over all the variables (here: 12) of all the other nuclei. The rather awkward experience of this "direct approach" suggests a challenge for the future, namely to search for additional relations between the density and flux density, beyond the continuity equation with corresponding boundary conditions, which would provide a convenient short-cut. As a bottom line, this field of research, intramolecular reduced nuclear flux densities, is heading for further significant progresses.

Acknowledgments

We would like to express our gratitude to the coauthors of Refs. 4–10, Dr Timm Bredtmann (MBI Berlin), Dr Christian Bressler (European XFEL, Hamburg), Dr Thomas Grohmann (Freie Universitiät Berlin, FUB), Prof. Hiroyuki Katsuki (Nara IST Ikoma), Prof. Hirohiko Kono (Tohoku University Sendai, TUS), Prof. Shiro Koseki (Osaka Prefecture University, Sakai), Mr Kosuke Nakamura (TUS), Prof. Kenji Ohmori (IMS Okazaki), Dr habil Burkhard Schmidt (FUB) for their important contributions and pleasant cooperations. Helpful and stimulating discussions with Prof. Dennis J. Diestler (University of Nebraska, Lincoln) and Prof. Beate Paulus (FUB) are also gratefully acknowledged. Our work profited from financial support (in alphabetical order of the list of the responsible co-authors) from Deutsche Forschungsgemeinschaft under grant No Ma 515/25-1, the Natural Science Foundation of Shanxi Province, China under Grant No. 20140221004, the talents program of Shanxi Province, and the National Natural Science Foundation of China under Grant No. 11004125.

References

1. E. Schrödinger, *Ann. Phys. (Leipzig)* **81**, 109 (1926).
2. D. J. Tannor, *Introduction to Quantum Mechanics — A Time-Dependent Perspective* (University Science Books, Sausalito, 2007).
3. N. E. Henriksen and F. Y. Hansen, *Theories of Molecular Reaction Dynamics — The Microscopic Foundation of Chemical Kinetics* (Oxford University Press, Oxford, 2008).
4. I. Barth, C. Bressler, S. Koseki and J. Manz, *Chem. Asian J.* **7**, 1261 (2012).

5. T. Bredtmann and J. Manz, *J. Chem. Sci.* **124**, 121 (2012).
6. T. Bredtmann, H. Kono, J. Manz, K. Nakamura and C. Stemmle, *ChemPhysChem* **14**, 1397 (2013).
7. T. Bredtmann, H. Katsuki, J. Manz, K. Ohmori and C. Stemmle, *Mol. Phys.* **111**, 1691 (2013).
8. T. Grohmann, J. Manz and A. Schild, *Mol. Phys.* **111**, 2251 (2013).
9. J. Manz, J. F. Pérez-Torres and Y. Yang, *Phys. Rev. Lett.* **111**, 153004 (2013).
10. J. Manz, A. Schild, B. Schmidt and Y. Yang, *Chem. Phys.* DOI: 10.1016/j.chemphys.2014.04.004 (2014).
11. I. Barth, J. Manz and P. Sebald, *Chem. Phys.* **346**, 89 (2008).
12. I. Barth, J. Manz, G. Pérez-Hernández and P. Sebald, *Z. Phys. Chem.* **222**, 13111 (2008).
13. I. Barth, H.-C. Hege, H. Ikeda, A. Kenfack, M. Koppitz, F. Marquardt and G. K. Paramonov, *Chem. Phys. Lett.* **481**, 118 (2009).
14. I. Barth and J. Manz, Quantum switching of magnetic fields by circulary polarized re-optimized π laser pulses: from one-electron atomic ions to molecules, Chapter 2, In *Progress in Ultrafast Intense Laser Science VI*, eds. K. Yamanouchi, A. D. Bandrauk and G. Gerber, Springer Series in Chemical Physics, Vol. 99 (Springer-Verlag, Berlin, 2010), pp. 21–44.
15. D. J. Diestler, *J. Phys. Chem. A* **116**, 2728 (2011).
16. D. J. Diestler, A. Kenfack, J. Manz and B. Paulus, *J. Phys. Chem. A* **116**, 2736 (2012).
17. I. Barth, *J. Phys. Chem. A* **116**, 11283 (2012).
18. D. J. Diestler, A. Kenfack, J. Manz, B. Paulus, J. Pérez-Torres and V. Pohl, *J. Phys. Chem. A* **117**, 8519 (2013).
19. J. F. Pérez-Torres, *Phys. Rev. A* **87**, 062512 (2013).
20. P. Lazzeretti, *Prog. Nucl. Magn. Reson. Spectrosc.* **36**, 1 (2000).
21. E. Steiner and P. Fowler, *J. Phys. Chem. A* **105**, 9553 (2001).
22. T. Heine, C. Corminboeuf and G. Seifert, *Chem. Rev.* **105**, 3889 (2005).
23. I. Barth and J. Manz, *Angew. Chem. Int. Ed.* **45**, 2962 (2006).
24. I. Barth, J. Manz, Y. Shigeta and K. Yagi, *J. Am. Chem. Soc.* **128**, 7043 (2006).
25. I. Barth, J. Manz and L. Serrano-Andrés, *Chem. Phys.* **347**, 263 (2008).
26. I. Barth, L. Serrano-Andrés and T. Seideman, *J. Chem. Phys.* **109**, 164303 (2008).
27. I. Barth, L. Serrano-Andrés and T. Seideman, *J. Chem. Phys.* **130**, Erratum: 109901 (2009).
28. M. Okuyama and K. Takatsuka, *Chem. Phys. Lett.* **476**, 109 (2009).
29. T. Yonehara and K. Takatsuka, *Chem. Phys.* **366**, 114 (2009).
30. K. Nagashima and K. Takatsuka, *J. Phys. Chem. A* **113**, 15240 (2009).
31. K. Takatsuka and T. Yonehara, *Adv. Chem. Phys.* **144**, 93 (2009).
32. K. Takatsuka and T. Yonehara, *Phys. Chem. Chem. Phys.* **13**, 4987 (2011).
33. M. Okuyama and K. Takatsuka, *Bull. Chem. Soc. Jpn.* **86**, 217 (2012).
34. K. Nagashima and K. Takatsuka, *J. Phys. Chem. A* **116**, 11167 (2012).
35. S. Patchkovskii, *J. Chem. Phys.* **137**, 084109 (2012).
36. H. Mineo, S. Lin and Y. Fujimura, *J. Chem. Phys.* **138**, 074304 (2013).
37. D. R. Herschbach, *Angew. Chem. Int. Ed.* (*Nobel lecture*) **26**, 1221 (1987).
38. Y. T. Lee, *Angew. Chem. Int. Ed.* (*Nobel lecture*) **26**, 939 (1987).

39. E. A. McCullough and R. E. Wyatt, *J. Chem. Phys.* **54**, 3578 (1971).
40. M. H. Alexander, *J. Chem. Phys.* **95**, 8931 (1991).
41. D. E. Manolopoulos and M. H. Alexander, *J. Chem. Phys.* **97**, 2527 (1992).
42. I. Barth and J. Manz, *Phys. Rev. A* **75**, 012510 (2007).
43. A. Accardi, I. Barth, O. Kühn and J. Manz, *J. Phys. Chem. A* **114**, 11252 (2010).
44. T. Frohnmeyer and T. Baumert, *Appl. Phys. B* **71**, 259 (2000).
45. T. Ergler, A. Rudenko, B. Feuerstein, K. Zrost, C. Schröter, R. Moshammer and J. Ullrich, *Phys. Rev. Lett.* **97**, 193001 (2006).
46. S. Chelkowski, T. Bredtmann and A. D. Bandrauk, *Phys. Rev. A* **85**, 033404 (2012).
47. H. C. Hege, J. Manz, F. Marquardt, B. Paulus and A. Schild, *Chem. Phys.* **376**, 46 (2010).
48. A. Kenfack, F. Marquardt, G. K. Paramonov, I. Barth, C. Lasser and B. Paulus, *Phys. Rev. A* **81**, 052502 (2010).
49. A. Kenfack, I. Barth, F. Marquardt and B. Paulus, *Phys. Rev. A* **82**, 062502 (2010).
50. D. Andrae, I. Barth, T. Bredtmann, H. C. Hege, J. Manz, F. Marquartd and B. Paulus, *J. Phys. Chem. B* **115**, 5476 (2011).
51. T. Bredtmann and J. Manz, *Angew. Chem. Int. Ed.* **50**, 12652 (2011).
52. J. Manz and K. Yamamoto, *Mol. Phys.* **110**, 517 (2012).
53. A. Kenfack, S. Banerjee and B. Paulus, *Phys. Rev. A* **85**, 032501 (2012).
54. T. Bredtmann, E. Hupf and B. Paulus, *Phys. Chem. Chem. Phys.* **14**, 15494 (2012).
55. T. Yamamoto, *J. Chem. Phys.* **33**, 281 (1960).
56. W. H. Miller, *J. Chem. Phys.* **61**, 1823 (1974).
57. W. H. Miller, S. D. Schwartz and J. W. Tromp, *J. Chem. Phys.* **79**, 4889 (1983).
58. W. H. Miller, *Acc. Chem. Res.* **26**, 174 (1993).
59. W. H. Miller, *J. Phys. Chem. A* **102**, 793 (1998).
60. U. Manthe, T. Seideman and W. H. Miller, *J. Chem. Phys.* **101**, 4759 (1994).
61. U. Manthe, *J. Chem. Phys.* **102**, 9205 (1995).
62. F. Matzkies and U. Manthe, *J. Chem. Phys.* **106**, 2646 (1997).
63. F. Matzkies and U. Manthe, *J. Chem. Phys.* **108**, 4828 (1998).
64. T. Wu, H. J. Werner and U. Manthe, *Science* **306**, 2227 (2004).
65. T. J. Park and J. C. Light, *J. Chem. Phys.* **88**, 4897 (1988).
66. D. H. Zhang and J. C. Light, *J. Chem. Phys.* **104**, 6184 (1996).
67. H. Katsuki, H. Chiba, B. Girard, C. Meier and K. Ohmori, *Phys. Rev. Lett.* **102**, 103602 (2009).
68. E. R. Hosler and S. Leone, *Phys. Rev. A* **88**, 023420 (2013).
69. C. Meier and V. Engel, *Chem. Phys. Lett.* **212**, 691 (1993).
70. A. Assion, M. Geisler, J. Helbing, V. Seyfried and T. Baumert, *Phys. Rev. A* **54**, R4605 (1996).
71. S. Chelkowski, P. Corkum and A. D. Bandrauk, *Phys. Rev. Lett.* **82**, 3416 (1999).
72. B. Feuerstein and U. Thumm, *Phys. Rev. A* **67**, 063408 (2003).
73. P. C. Morse and H. Feshbach, *Methods of Theoretical Physics* (McGraw-Hill, New York, 1953).
74. F. Martin, R. Bacis, S. Churassy and J.Vergès, *J. Mol. Spectrosc.* **116**, 71 (1986).
75. R. F. Barrow and K. K. Yee, *J. Chem. Soc. Faraday Trans. II* **69**, 684 (1973).

76. I. S. Averbukh, M. J. J. Vrakking, D. M. Villeneuve and A. Stolow, *Phys. Rev. Lett.* **77**, 3518 (1996).
77. T. Lohmüller, V. Engel, J. Beswick and C. Meier, *J. Chem. Phys.* **120**, 10442 (2004).
78. T. Bredtmann and B. Paulus, *J. Chem. Theory Comp.* **9**, 3026 (2013).
79. D. Luckhaus, *J. Chem. Phys.* **113**, 1329 (2000).
80. R. Marquardt, M. Quack, I. Thanopulos and D. Luckhaus, *J. Chem. Phys.* **118**, 643 (2003).
81. R. Marquardt, K. Sagui, W. Klopper and M. Quack, *J. Phys. Chem. B* **109**, 8439 (2005).
82. Y. Fujimura, L. González, K. Hoki, D. Kröner, J. Manz and Y. Ohtsuki, *Angew. Chem. Int. Ed.* **39**, 4586 (2000).
83. M. Shapiro, E. Frishman and P. Brumer, *Phys. Rev. Lett.* **84**, 1669 (2000).
84. P. Brumer, E. Frishman and M. Shapiro, *Phys. Rev. A* **65**, 015401 (2001).
85. E. Frishman, M. Shapiro, D. Gerbasi and P. Brumer, *J. Chem. Phys.* **119**, 7237 (2003).
86. P. Král, I. Thanopulos, M. Shapiro and D. Cohen, *Phys. Rev. Lett.* **90**, 033001 (2003).
87. D. Gerbasi, P. Brumer, I. Thanopulos, P. Král and M. Shapiro, *J. Chem. Phys.* **120**, 11557 (2004).
88. D. Gerbasi, M. Shapiro and P. Brumer, *J. Chem. Phys.* **124**, 074315 (2006).
89. K. Hoki, D. Kröner and J. Manz, *Chem. Phys.* **267**, 59 (2001).
90. T. Klamroth and D. Kröner, *J. Chem. Phys.* **129**, 234701 (2008).
91. D. Kröner, B. Klaumünzer and T. Klamroth, *J. Phys. Chem. A* **112**, 9924 (2008).
92. J. R. Letelier and C. A. Utreras-Dias, *Spectrochim. Acta A, Mol. Biomol. Spectrosc.* **53**, 247 (1997).
93. I. Iwakura, A. Yabushita and T. Kobayashi, *Chem. Lett.* **39**, 374 (2010).
94. I. Iwakura, A. Yabushita, J. Liu, K. Okamura and T. Kobayashi, *Phys. Chem. Chem. Phys.* **124**, 121 (2012).
95. D. J. Tannor and S. A. Rice, *J. Chem. Phys.* **83**, 5013 (1985).
96. A. P. Peirce, M. A. Dahleh and H. Rabitz, *Phys. Rev. A* **37**, 4950 (1988).
97. W. Jakubetz, J. Manz and H.-J. Schreier, *Chem. Phys. Lett.* **165**, 100 (1990).
98. S. A. Rice and M. Zhao, *Optimal Control of Molecular Dynamics* (Wiley, New York, 2003).
99. M. Shapiro and P. Brumer, *Quantum Control of Molecular Processes*, 2nd edn (Wiley-VCH, Weinheim, 2012).
100. D. Bohm, *Phys. Rev.* **85**, 180 (1952).
101. R. E. Wyatt, *Quantum Dynamics with Trajectories, Introduction to Quantum Hydrodynamics* (Springer, New York, 2003).
102. H. G. Winful, *Phys. Rep.* **436**, 1 (2006).
103. S. Haroche, *Rev. Mod. Phys.* (*Nobel lecture*) **85**, 1083 (2013).
104. M. Barbatti, S. Belz, M. Leibscher, H. Lischka and J. Manz, *Chem. Phys.* **350**, 15 (2008).
105. I. Barth, Quantum control of electron and nuclear circulations, ring currents, and induced magnetic fields in atoms, ions, and molecules by circularly polarized laser pulses, Ph.D. thesis, Freie Universität Berlin, Germany (2009), http://www.diss.fu-berlin.de/diss/receive/FUDISS_thesis_00000010586.
106. B. O. Roos, P. R. Taylor and P. E. Siegbahn, *Chem. Phys.* **48**, 157 (1980).

107. K. Andersson, P. Å. Malmqvist, B. O. Roos, A. J. Sadlej and K. Wolinski, *J. Phys. Chem.* **94**, 5483 (1990).
108. K. Andersson, P. Å. Malmqvist and B. O. Roos, *J. Chem. Phys.* **96**, 1218 (1992).
109. B. O. Roos, R. Lindh, P. Å. Malmqvist, V. Veryazov and P. O. Widmark, *J. Phys. Chem. A* **109**, 6575 (2005).
110. M. Douglas and N. M. Kroll, *Ann. Phys.* **82**, 89 (1974).
111. B. A. Hess, *Phys. Rev. A* **33**, 3742 (1986).
112. Molcas: Release 7.0. K. Andersson, F. Aquilante, M. Barysz, E. Bednarz, A. Bernhardsson, M. R. A. Blomberg, Y. Carissan, D. L. Cooper, M. Cossi, A. Devarajan, L. De Vico, N. Ferré, M. P. Fülscher, A. Gaenko, L. Gagliardi, G. Ghigo, C. de Graaf, B. A. Hess, D. Hagberg, A. Holt, G. Karlström, J. W. Krogh, R. Lindh, P.-Å. Malmqvist, T. Nakajima, P. Neogrády, J. Olsen, T. B. Pedersen, J. Raab, M. Reiher, B. O. Roos, U. Ryde, I. Schapiro, B. Schimmelpfennig, M. Schütz, L. Seijo, L. Serrano-Andrés, P. E. M. Siegbahn, J. Sålring, T. Thorsteinsson, V. Veryazov, P.-O. Widmark and A. Wolf, Department of Theoretical Chemistry, Lund University, Sweden (2007).
113. I. Barth and C. Lasser, *J. Phys. B* **42**, 235101 (2009).
114. W. H. Shaffer, *Rev. Mod. Phys.* **16**, 245 (1944).

ADVANCES IN MULTI-PHOTON PROCESSES AND SPECTROSCOPY

Volume 22

Edited by

S. H. Lin
National Chiao-Tung University, TAIWAN
Institute of Atomic and Molecular Sciences, TAIWAN
and Arizona State University, USA

A. A. Villaeys
Institute de Physique et Chimie des
Matériaux de Strasbourg, FRANCE

Y. Fujimura
Tohoku University, JAPAN

World Scientific

NEW JERSEY · LONDON · SINGAPORE · BEIJING · SHANGHAI · HONG KONG · TAIPEI · CHENNAI

Published by

World Scientific Publishing Co. Pte. Ltd.

5 Toh Tuck Link, Singapore 596224

USA office: 27 Warren Street, Suite 401-402, Hackensack, NJ 07601

UK office: 57 Shelton Street, Covent Garden, London WC2H 9HE

British Library Cataloguing-in-Publication Data
A catalogue record for this book is available from the British Library.

Library of Congress Control Number: 86643116

Advances in Multi-Photon Processes and Spectroscopy — Vol. 22
ADVANCES IN MULTI-PHOTON PROCESSES AND SPECTROSCOPY
(Volume 22)

Copyright © 2015 by World Scientific Publishing Co. Pte. Ltd.

All rights reserved. This book, or parts thereof, may not be reproduced in any form or by any means, electronic or mechanical, including photocopying, recording or any information storage and retrieval system now known or to be invented, without written permission from the publisher.

For photocopying of material in this volume, please pay a copying fee through the Copyright Clearance Center, Inc., 222 Rosewood Drive, Danvers, MA 01923, USA. In this case permission to photocopy is not required from the publisher.

ISBN 978-981-4619-03-5

Typeset by Stallion Press
Email: enquiries@stallionpress.com

Printed in Singapore